Draft version October 23, 2017
Preprint typeset using LaTeX style emulateapj v. 12/16/11

THE PARSEC-SCALE RELATIONSHIP BETWEEN I_{CO} AND A_V IN LOCAL MOLECULAR CLOUDS

Cheoljong Lee[1], Adam K. Leroy[2], Alberto D. Bolatto[3], Simon C. O. Glover[4], Remy Indebetouw[5,6], Karin Sandstrom[7], and Andreas Schruba[8]

Draft version October 23, 2017

ABSTRACT

We measure the parsec-scale relationship between integrated CO intensity (I_{CO}) and visual extinction (A_V) in 24 local molecular clouds using maps of CO emission and dust optical depth from *Planck*. This relationship informs our understanding of CO emission across environments, but clean Milky Way measurements remain scarce. We find uniform I_{CO} for a given A_V, with the results bracketed by previous studies of the Pipe and Perseus clouds. Our measured $I_{CO}-A_V$ relation broadly agrees with the standard Galactic CO-to-H_2 conversion factor, the relation found for the Magellanic clouds at coarser resolution, and numerical simulations by Glover & Clark (2016). This supports the idea that CO emission primarily depends on shielding, which protects molecules from dissociating radiation. Evidence for CO saturation at high A_V and a threshold for CO emission at low A_V varies remains uncertain due to insufficient resolution and ambiguities in background subtraction. Resolution of order 0.1 pc may be required to measure these features. We use this $I_{CO}-A_V$ relation to predict how the CO-to-H_2 conversion factor (X_{CO}) would change if the Solar Neighborhood clouds had different dust-to-gas ratio (metallicity). The calculations highlight the need for improved observations of the CO emission threshold and HI shielding layer depth. They are also sensitive to the shape of the column density distribution. Because local clouds collectively show a self-similar distribution, we predict a shallow metallicity dependence for X_{CO} down to a few tenths of solar metallicity. However, our calculations also imply dramatic variations in cloud-to-cloud X_{CO} at subsolar metallicity.

Subject headings: Galaxy : ISM – (galaxy:) galaxy – (ISM:) dust, extinction – ISM:clouds – ISM: molecules

1. INTRODUCTION

CO emission is the main observational tracer of molecular gas in the Milky Way and other galaxies. To use this tracer effectively, we must understand the origin of CO emission in molecular clouds, the relationship between CO emission and H_2 mass, and how these vary among different environments. A key aspect of this variation is how the CO-to-H_2 conversion factor (X_{CO}; defined as the ratio between the column density of molecular hydrogen, N_{H_2}, and the integrated CO intensity, I_{CO}) depends on metallicity (see review in Bolatto et al. 2013).

Lee et al. (2015) proposed that a productive way to approach this topic is to consider CO emission from a molecular cloud or an ensemble of clouds as the product of several separable phenomena: (1) the probability distribution function (PDF) of gas column densities within a cloud, (2) the local dust-to-gas ratio which relates a gas column density to a dust column density, (3) the relationship between dust column density and CO emission, and (4) the importance of HI shielding envelopes at low gas column density and low dust abundance (e.g., Lee et al. 2012, 2014). Lee et al. showed how combining these empirical relationships allow one to predict a scaling for X_{CO} as a function of metallicity.

The major advantage of this approach is that each of these parts is a significant topic of research with its own literature, and that each of these topics can be constrained by observations. For example, the column density PDF of local molecular clouds has been studied by, e.g., Kainulainen et al. (2009); Lombardi et al. (2015); Schneider et al. (2015); Abreu-Vicente et al. (2015). The dependence of the dust-to-gas ratio on metallicity has been examined in nearby spiral and dwarf galaxies by, e.g., Sandstrom et al. (2013); Rémy-Ruyer et al. (2014). The relationship between dust column density and CO emission has been studied by, e.g., Lombardi et al. (2006); Pineda et al. (2008); Lee et al. (2015). And the HI−H_2 balance in molecular clouds has been examined by, e.g., Krumholz et al. (2009); Lee et al. (2012, 2014); Sternberg et al. (2014).

These individual topics are more tractable to observational studies than a direct estimate of the H_2 mass. This is especially true in low metallicity dwarf galaxies where the necessary observations remain difficult to obtain and systematic biases affect all available techniques (Bolatto et al. 2013). Studies targeting these four individual phenomena separately can be constructed more cleanly, and make valuable contributions to our understanding of the H_2 content in (low metallicity) galaxies.

[1] Department of Astronomy, University of Virginia, Charlottesville, VA 22904, USA
[2] Department of Astronomy, The Ohio State University, 140 West 18th Avenue, Columbus, OH, 43210, USA
[3] Department of Astronomy, Laboratory for Millimeter-wave Astronomy, and Joint Space Institute, University of Maryland, College Park, Maryland 20742, USA
[4] Institute für theoretische Astrophysik, Zentrum für Astronomie der Universität Heidelberg, Albert-Ueberle Str. 2, 69120 Heidelberg, Germany
[5] Department of Astronomy, University of Virginia, Charlottesville, VA 22904, USA
[6] National Radio Astronomy Observatory, 520 Edgemont Rd, Charlottesville, VA 22903, USA
[7] Center for Astrophysics and Space Sciences, Department of Physics, University of California, San Diego, 9500 Gilman Drive, La Jolla, CA 92093, USA
[8] Max-Planck-Institut für extraterrestrische Physik, Giessenbachstraße 1, 85748 Garching, Germany

Thus, the simple, separable approach of Lee et al. (2015) represents a practical way to make progress towards understanding the metallicity dependence of $X_{\rm CO}$ based on observations. It offers a natural way to fold in our knowledge of ISM structure, dust physics, and PDR structure. As this knowledge improves, so does our understanding of $X_{\rm CO}$.

The lynchpin of this approach is the ability to predict CO emission from the line of sight dust extinction (expressed as V-band extinction, $A_{\rm V}$), or dust column density, through a part of a molecular cloud. Dust is the primary agent shielding CO molecules against dissociating radiation, and thus defines the part of a cloud in which CO represents the dominant form of carbon. Based on this, one can expect that dust shielding is a reasonable tracer of CO emission, at least to first order. To second order, variations in physical conditions such as gas temperature, turbulence, CO opacity, self-shielding, cloud geometry, and the external radiation field may complicate the relationship.

Only two Milky Way clouds—the Perseus and Pipe molecular clouds—have been well-studied in the $I_{\rm CO}-A_{\rm V}$ parameter space (Lombardi et al. 2006; Pineda et al. 2008; Lee et al. 2014); though many studies related to this topic have been carried out going back to the earliest CO studies. The observational studies by Lombardi et al. (2006), Pineda et al. (2008), and Lee et al. (2014) show a clear relationship between $A_{\rm V}$ and $I_{\rm CO}$ within a molecular cloud. A similar relationship is predicted by analytic models of photon dominated regions (PDRs; e.g., Maloney & Black 1988; van Dishoeck & Black 1988; Lequeux et al. 1994; Bell et al. 2006; Wolfire et al. 2010), and in simulations that model chemistry and radiative transfer in turbulent clouds (Glover & Mac Low 2011; Shetty et al. 2011; Glover & Clark 2012a).

Motivated by these observational and theoretical works, Lee et al. (2015) studied the relationship between CO emission and dust extinction in three Local Group galaxies with different metallicities, aiming to test this simple picture (see also Imara & Blitz 2007; Leroy et al. 2009). On the scale of a large part of a molecular cloud, $\sim$10 pc, they found that the Large Magellanic Cloud (LMC) and Small Magellanic Cloud (SMC) have similar $I_{\rm CO}$ for a given $A_{\rm V}$ as nearby Milky Way clouds (with $A_{\rm V}$ derived from the far infrared dust emission spectral energy distribution). The agreement in the $I_{\rm CO}-A_{\rm V}$ relationship over a metallicity range of $\sim 0.2-1\ Z_{\odot}$ suggests a common relationship between CO and dust shielding across galaxies. Although the 10 pc spatial scales analyzed by Lee et al. (2015) are coarse, one may expect a similar dependence of CO emission on dust shielding to hold at higher resolution (i.e., on the scale of cloud substructures). This underpins the idea of the simple four-step approach to determine the metallicity dependence of $X_{\rm CO}$ as introduced in Lee et al. (2015).

Thus, a better understanding of how to predict CO emission from line of sight extinction in *resolved* molecular clouds can help improve our understanding of $X_{\rm CO}$. The fact that only two Milky Way clouds have been characterized in the $I_{\rm CO}-A_{\rm V}$ relationship at parsec-scale resolution limits our ability to understand CO emission from more extreme environments. Although the local molecular cloud population has been studied extensively, including many studies of $X_{\rm CO}$ (e.g., Pineda et al. 2008, 2010), this specific, very useful measurement—the $I_{\rm CO}-A_{\rm V}$ relationship between line of sight CO intensity and dust extinction—has not been systematically carried out.

In this paper, we take advantage of the new all-sky CO and dust extinction maps from the *Planck* mission (Planck Collaboration et al. 2013a,b) to characterize this relationship at $\sim$1 pc resolution for 24 local molecular clouds. We present the average $I_{\rm CO}-A_{\rm V}$ relationship, measure the scatter about this relation, and the differences from cloud to cloud. We assess the uncertainty due to foreground and background contamination, and compare our observations with numerical simulations from Glover & Clark (2016). Our goal is to create a point of reference for CO and dust studies of other galaxies by analyzing in detail local molecular clouds in the Milky Way.

2. DATA

We use the *Planck* all-sky CO (Planck Collaboration et al. 2013a) and E(B−V) (Planck Collaboration et al. 2013b) maps to measure the $I_{\rm CO}-A_{\rm V}$ relationship in local molecular clouds. We consider the clouds listed in Table 1 of Dame et al. (2001), supplemented by a few other well-known nearby regions. Table 1 lists our targets, and Figure 1 shows their location on the *Planck* CO map of the Milky Way.

2.1. *CO Map*

The *Planck* team provided three different types of CO maps, all extracted from the HFI broadband photometric data at 100, 217, and 353 GHz (Planck Collaboration et al. 2013a). In this paper, we use the "TYPE 1" CO 1-0 map, which is generated by the single-channel method (see Section 4.2.1 of their paper for more information). This map has a lower signal-to-noise (S/N) ratio than the other map types, but it suffers less from foreground and background contamination. As we are interested in molecular clouds near the Galactic plane, we expect contamination to be a major issue and choosing the TYPE 1 map significantly improves the fidelity of our results.

The native angular resolution of the *Planck* TYPE 1 CO map is 9.65′. We convolve this map using a Gaussian kernel to 18′ in order to improve the S/N ratio. At the typical distance of $\sim$200 pc for our cloud sample, this corresponds to $\sim$1 pc spatial resolution. The *Planck* TYPE 1 CO map includes a contribution from ^{13}CO. We correct for this by dividing the provided map by 1.11, assuming a constant ^{13}CO/^{12}CO ratio following Planck Collaboration et al. (2013a). After correction, we compared the *Planck* CO map with the all-sky CO map by Dame et al. (2001) along lines of sight toward the molecular clouds considered in our analysis. The two maps appear almost identical in those regions. Planck Collaboration et al. (2013a) report the typical 1σ uncertainty of the CO map to be approximately 1.77 K km s^{-1} at 15′ resolution, with $\sim$10 per cent absolute calibration uncertainty due to ^{13}CO contamination. We prefer the *Planck* CO maps because of their better angular resolution and wider sky coverage, but expect that we would have reached the same result using the Dame et al. (2001) map.

2.2. $A_{\rm V}$ *Maps*

TABLE 1
GALACTIC MOLECULAR CLOUDS CONSIDERED IN OUR ANALYSIS

Cloud	l (degrees)	b (degrees)	width (degrees)	height (degrees)	distance (parsecs)	physical resolution (parsecs)	$\langle \Delta A_V \rangle^a$ (mag)
Aquila South	34.5	-16.5	6.0	4.5	110.0[b]	0.6	0.4
California	161.0	-9.0	5.5	5.0	410.0[b]	2.1	1.3
Camelopardalis	148.0	20.0	6.0	6.0	200.0[b]	1.0	0.3
Canis Major	224.0	-2.0	4.0	2.0	1150.0[c]	6.0	2.8
Cepheus North	118.0	16.2	5.0	2.0	360.0[b]	1.9	0.8
Cepheus South	118.0	12.7	5.0	1.5	900.0[b]	4.7	1.3
Chamaeleon	299.0	-15.5	7.0	8.0	150.0[d]	0.8	0.5
Gem OB1	191.5	0.5	5.0	5.0	2000.0[e]	10.5	2.2
Gum Nebula	266.0	-10.0	5.0	5.0	450.0[f]	2.4	0.8
Hercules	44.5	9.0	3.5	3.0	200.0[b]	1.0	0.8
Lacerta	102.0	-14.5	7.5	6.5	510.0[b]	2.7	0.5
Lupus	341.0	13.5	8.0	11.0	155.0[g]	0.8	0.8
Mon OB1	201.5	2.5	5.0	3.5	890.0[b]	4.7	2.1
Mon R2	217.0	-12.0	5.0	5.0	905.0[c]	4.7	0.9
Ophiuchus	358.0	16.0	10.0	8.0	125.0[b]	0.7	0.8
Orion A	210.0	-19.0	7.0	2.0	371.0[c]	2.0	0.4
Orion B	205.5	-11.0	4.5	6.0	398.0[c]	2.1	1.1
Pipe Nebula	0.0	5.5	4.0	3.0	130.7[g]	0.7	2.1
Pegasus	95.0	-34.0	12.0	9.0	230.0[b]	1.2	0.2
Perseus	160.0	-20.0	5.0	5.0	240.0[h]	1.3	0.5
Polaris Flare	123.0	26.0	6.0	6.0	380.0[b]	2.0	0.2
R Coronae Australis	5.0	-23.0	10.0	9.0	130.0[i]	0.7	0.2
Rosette	207.0	-2.0	2.0	2.0	1330.0[c]	7.0	2.8
Taurus	172.5	-15.0	7.5	5.0	135.0[b]	0.7	1.0

[a] Mean value of background subtraction across the cloud, estimated from the reference region. [b] Schlafly et al. (2014) [c] Lombardi et al. (2011) [d] Boulanger et al. (1998) [e] Carpenter et al. (1995) [g] Lombardi et al. (2008) [h] Lombardi et al. (2010) [i] Reipurth (2008)

To estimate a dust extinction, A_V, map for each cloud, we use a version of the dust reddening, E(B−V), map provided by the *Planck* team (Planck Collaboration et al. 2013b). We use a simple conversion of their dust optical depth at 850 μm (τ_{850}), which is the result of a modified blackbody fit to the infrared and sub-millimeter SED. Planck Collaboration et al. (2013b) found a strong correlation between E(B−V) from SDSS quasar studies and dust optical depth for diffuse lines of sight at high Galactic latitude (E(B−V) < 0.1, see their Figure 22). We adopt their best fit, $\mathrm{E(B-V)} = 1.49 \times 10^4\ \tau_{850}$. We multiply then by $R_V = 3.1$ to obtain the dust extinction, A_V.

We expect this conversion from τ_{850} to A_V to appropriate for the diffuse ISM, but to also have some dependence on environment. Studying the Taurus molecular clouds, the *Planck* team found the *Planck* E(B−V) from τ_{850} to be ∼25% higher than the E(B−V) derived from the NIR color excess method. We expect that a similar uncertainty in the translation to A_V may exist in the other molecular clouds. Nevertheless, the correlations between the NIR-based E(B−V) map and the *Planck* E(B−V) map are quite strong (see Table 5 in Planck Collaboration et al. 2013b). We expect that the qualitative features of our results (e.g. the shape of $I_{CO}-A_V$ relation) remain reliable, as long as dust optical properties do not change much within a molecular cloud. Similarly, our expressed A_V may shift if one applies a higher R_V but only differential changes within a cloud will affect the shape of our results. Still, we caution that the rigorous way to read our results is as a correlation between I_{CO} and dust optical depth, τ_{850}, which is closely related to the dust column density.

The angular resolution of the *Planck* E(B−V) map is 5′. We degrade this resolution to match that of the CO map. The fractional uncertainty in τ_{850} at its native resolution is about 10 per cent in diffuse regions and typically 2−5 per cent in infrared-bright regions (Planck Collaboration et al. 2013b). However, the systematic uncertainty associated with converting τ_{850} to A_V and removing the foreground and background contamination is larger.

2.3. *Contamination Subtraction from A_V Maps*

We aim to measure the amount of dust shielding column associated with a molecular cloud along each line of sight and compare it to the CO emission from the same cloud along the same line of sight. Unfortunately, our location within the Galaxy and the lack of velocity information for the dust continuum make it difficult to separate the emission associated with the molecular cloud from background and foreground emission (for a rare exception that proves the rule, see Lee et al. 2014). This difficulty also represents one of the major obstacles to accurate measurements of the column density PDF in molecular clouds using dust continuum emission. In that context, the issue has been discussed and solutions have been proposed in several recent papers including Lombardi et al. (2015) and Schneider et al. (2015).

Here, we adopt a simple approach to correct for the foreground and background contamination, following Schneider et al. (2015) with slight modifications. The basic idea is to calculate the level of contamination from the sky near the cloud. To define a reference region, we consider an area that extends twice the length of the nominal cloud region (Table 1) in Galactic latitude. Next,

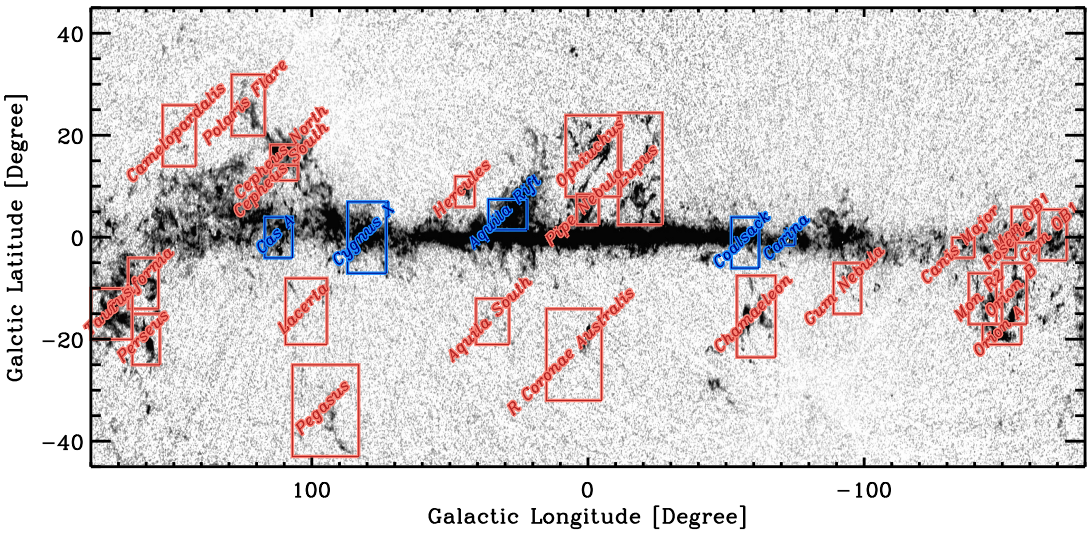

FIG. 1.— Molecular clouds studied in this paper, highlighted on the *Planck* CO map. The rectangles show the regions where we estimate the foreground and background dust column for each molecular cloud. We include only the clouds enclosed by red rectangles in our main analysis. We attempted measurements for clouds marked with blue rectangles, but found them to have too much uncertainty in the foreground and background to yield a reliable dust extinction measurement.

we mask the cloud region as well as any CO-bright regions outside the cloud (see Figure 2). The remaining unmasked lines of sight represent the sky near the molecular cloud without significant contribution from other molecular clouds.

Schneider et al. (2015) adopt a singe value of A_V, usually the minimum in the reference region, to represent the contamination for a given cloud. We modify this approach to allow the level of contamination to depend on Galactic latitude. This reflects the fact that clouds near the Galactic plane show a strong gradient in their level of contamination with Galactic latitude. This matches the expectation as the path length through the disk increases rapidly as one goes from high Galactic latitude toward the Galactic plane.

To calculate this latitude-dependent level of contamination, we measure the 25th percentile A_V value in each 0.5 degree-wide horizontal stripe of the reference region. We take this value as a representative dust contamination level for parts of the cloud with the same Galactic latitude. Then, we subtract this contamination from the *Planck* A_V map to isolate the A_V that belongs to the targeted cloud. We report the average A_V contamination for each cloud in Table 1.

We tried different statistics (e.g., median, mean, etc.) to measure the level of contamination. As the bottom right panel in Figure 2 illustrates, the largest difference is between doing nothing (the purple line) and doing something (the other lines). The choice of statistic plays a secondary role, and taking the 25th percentile in the reference region appears to be a good compromise. This avoids the case of widespread negative values of A_V in the cloud, which can occur using the mean or median (50th percentile). This may be due to imperfect masking, e.g., if the reference region contains some lines of sight associated with the molecular cloud complex even when masking additional CO-bright regions. Or it may stem from other clouds overlapping with the reference region. Overall, the choice of statistic for background subtraction has a minor impact on our results compared to other factors like the choice of reference region (see the discussion in Schneider et al. 2015).

TABLE 2
I_{CO} AT A GIVEN A_V IN GALACTIC MOLECULAR CLOUDS

Cloud	A_V (mag)	I_{CO} (K km s^{-1})
Aquila South	0.25	0.2 ± 1.2
Aquila South	0.50	0.6 ± 1.4
Aquila South	0.75	1.4 ± 1.6
Aquila South	1.00	2.2 ± 1.7
Aquila South	1.25	2.3 ± 1.0
Aquila South	1.50	0.8 ± 0.8
California	0.25	0.7 ± 1.6
California	0.50	1.5 ± 2.0
California	0.75	2.7 ± 2.1
California	1.00	3.9 ± 2.5
California	1.25	5.1 ± 2.9
...	...	...

NOTE. — This is a stub. The full data are available as a machine readable table distributed with the paper. Mean and scatter of I_{CO} in 0.25 mag wide bins of A_V estimated from τ_{850}. We report results for bins with at least 6 data points.

3. RESULTS

3.1. $I_{CO}-A_V$ *Relation for Individual Nearby Clouds*

Figure 1 shows the location of the clouds studied in this work, overlaid on the *Planck* Galactic CO map. Clouds shown in blue boxes were initially considered but excluded from the sample because of heavy contamination. Other than these, most of the clouds are located well outside of the Galactic plane, making it easier to compare the line of sight dust extinction and integrated CO intensity. Our cloud sample includes the two molecular clouds, the Pipe Nebula and Perseus molecular cloud, in which the $I_{CO}-A_V$ relationship has been measured by previ-

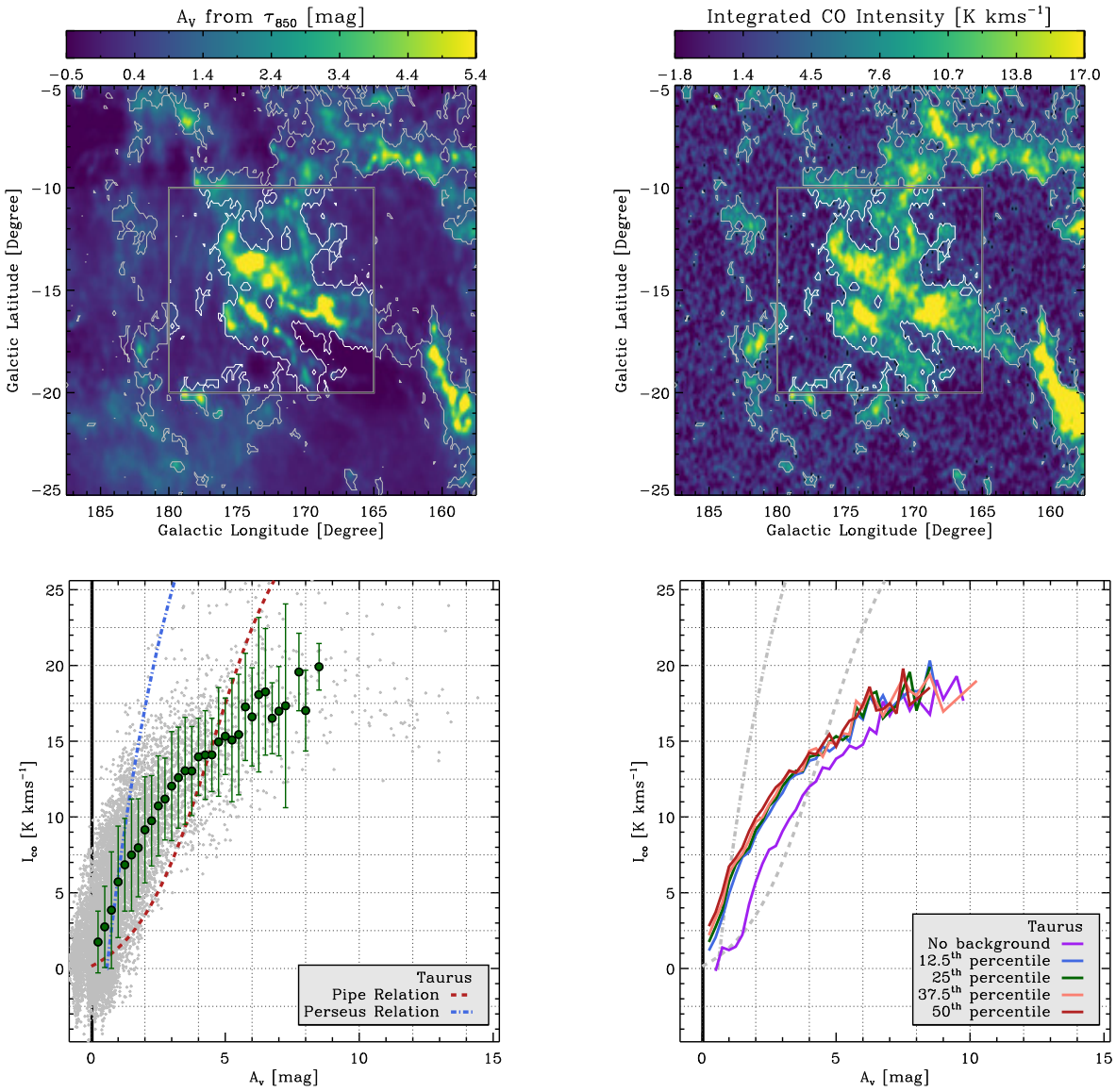

FIG. 2.— The distribution of dust extinction (*top left*), integrated CO intensity (*top right*), and the relationship between the two (*bottom left and bottom right*) in the Taurus molecular cloud. The rectangle in the upper panels indicates the "cloud" region used for the measurement. The white and gray contours mark the region of bright CO emission (S/N > 3). We estimate the contribution of foreground and background dust emission not associated with the cloud outside the marked rectangular region, also excluding the CO-bright regions. The bottom left panel shows the $I_{CO}-A_V$ relationship after background subtraction (Section 2.3). Here, the gray points are individual lines of sight and the green circles are the binned profile treating A_V as an independent variable. Error bars show $\pm 1\sigma$ scatter about the mean in each bin, and the black line indicates five times the rms A_V fluctuations in the background region. The bottom right panel shows the same binned profile constructed using different methods for background subtraction: no subtraction (purple) and then varying the level used for the subtraction about our fiducial 25th percentile case. In both panels, we plot the sub-parsec $I_{CO}-A_V$ relation for the Pipe Nebula (Lombardi et al. 2006) and the Perseus molecular cloud (Pineda et al. 2008).

ous works (Lombardi et al. 2006; Pineda et al. 2008; Lee et al. 2014). Although at coarser spatial resolution than these previous studies, we here increase the number of clouds with a parsec-scale measurement of the $I_{CO}-A_V$ relationship by an order of magnitude (from two to 24). Doing so, we attempt to distill a general relationship for local molecular clouds, capture the intrinsic spread, and search for physical variations between clouds. Figure 2 shows an example of our analysis for the Taurus molecular cloud. Similar figures for the other clouds can be found in the Appendix. In the top panels, we plot the maps of estimated visual extinction (A_V) and integrated CO intensity (I_{CO}). We find general coincidence between the location of bright CO emission and highly shielded lines of sight in the cloud region (marked with a black rectangle). This agrees qualitatively with the theoretical picture that shielding from the dissociating radiation by dust is the main factor in setting the extent of widespread CO emission (e.g, Wolfire et al. 2010; Glover & Mac Low 2011).

The bottom left panel shows the $I_{CO}-A_V$ relationship for Taurus. We plot integrated CO intensity as a function of line of sight dust extinction, with individual ∼1 pc diameter lines of sight shown as gray points. The ensemble of individual lines of sight show large scatter, far greater than the observational uncertainties. This

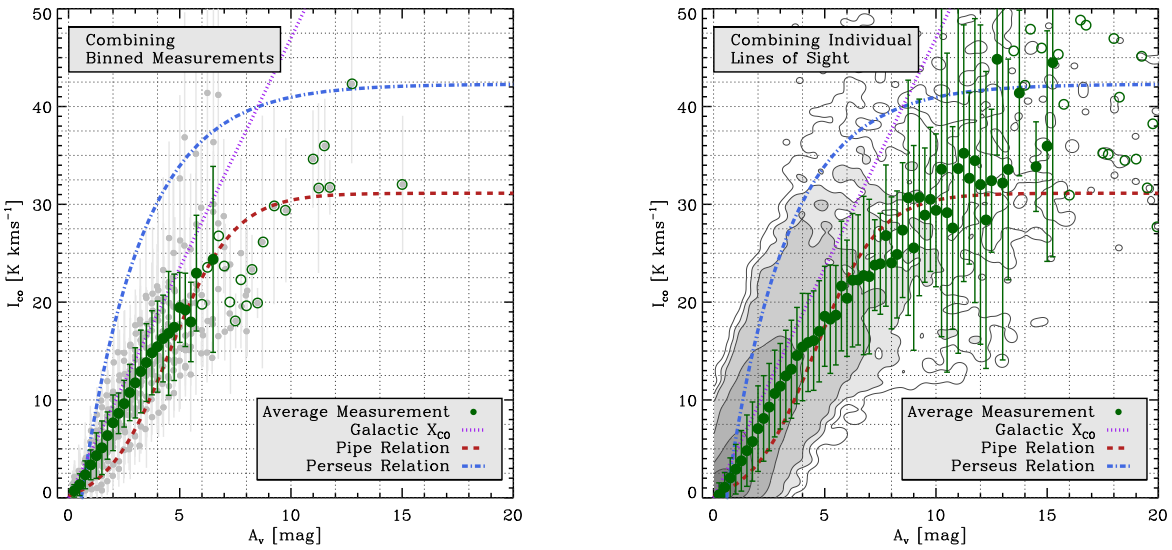

FIG. 3.— $I_{\rm CO}$ as a function of $A_{\rm V}$ combining the 24 local molecular clouds listed in Table 1. (*left*) The average relation calculated by combining the relations for the individual clouds. Each gray point here shows a bin from an individual cloud; the green profile shows the mean and scatter among the profiles. This approach weights each cloud equally. Unfilled circles mark the average $I_{\rm CO}$ in the $A_{\rm V}$ bins where we do not have enough statistics to estimate the scatter. (*right*) The average relation, now calculated treating each line of sight in the sample equally, so that larger clouds contribute more. The gray contours show data density and are chosen to encompass 99.9%, 99.5%, 99%, 95%, 75%, and 50% of the data. The green points again show the mean relation and the error bars indicate the 1σ scatter in the bin. Blue and red lines show the sub-parsec resolution $I_{\rm CO}-A_{\rm V}$ relations measured for the Pipe Nebula (Lombardi et al. 2006) and Perseus molecular cloud (Pineda et al. 2008).

is somewhat expected not only from the local variation of physical conditions (e.g., temperature, radiation field, turbulence) within a cloud (see Pineda et al. 2008), but also due to complex cloud geometry and projection effects. Physically, we expect that the CO abundance at any given point in a cloud will depend on a weighted average of the dust column in different directions from that point to the edge of the cloud, whereas we measure only the dust column along a single line of sight. Numerical simulations of turbulent molecular clouds find that although these quantities are correlated, there is considerable scatter in this relationship (see e.g. Clark & Glover 2014), potentially explaining much of the scatter in the observed $I_{\rm CO}-A_{\rm V}$ relationship.

To distill a representative relationship, we calculate the average $I_{\rm CO}-A_{\rm V}$ relation in each cloud by combining many lines of sight. Doing so, we treat $A_{\rm V}$ as the independent variable and estimate the median and standard deviation of integrated CO intensity in bins of $A_{\rm V}$. In Figure 2, this binned profile appears as the green circles with error bars indicating the rms (1σ) scatter of the CO emission within a given $A_{\rm V}$ bin. For comparison, we also plot the $I_{\rm CO}-A_{\rm V}$ relationships in the Pipe Nebula (dashed line; Lombardi et al. 2006) and Perseus molecular cloud (dash-dotted line; Pineda et al. 2008) measured at sub-parsec scales.

In Table 2, we report the average integrated CO intensity in bins of $A_{\rm V}$ for each cloud. We present results for $A_{\rm V}$ bins in which there are enough pixels ($n_{\rm pix} > 6$) to calculate the mean $I_{\rm CO}$ and the standard deviation about this value. Generally, we find that $I_{\rm CO}$ increases with increasing $A_{\rm V}$ in our clouds, though there is non-negligible scatter both among clouds and within individual clouds. Qualitatively, some of the clouds show hints of a minimum $A_{\rm V}$ threshold for detectable CO emission ($A_{\rm V,\,thres}$) or a saturation of CO emission at high $A_{\rm V}$, but not all clouds exhibit the same features. We come back to this point in Section 4.2 where we compare the $I_{\rm CO}-A_{\rm V}$ relationships among clouds, focusing on their various shapes.

Although we treat $A_{\rm V}$ as an independent variable, we emphasize that our derived $I_{\rm CO}-A_{\rm V}$ relation remains uncertain along the x-axis ($A_{\rm V}$) for several reasons. Key uncertainties, discussed above, include spatial variations in dust emissivity (which relates dust optical depth, τ, to dust extinction, $A_{\rm V}$) and uncertainty in the removal of foreground and background contamination. Furthermore, even if we estimate $A_{\rm V}$ perfectly, our measured relationship may not perfectly reflect the physical relationship between dust extinction and CO emission. As mentioned, cloud geometry complicates the ability to relate line of sight dust to the true shielding layer. Finally, although we convert dust optical depth to E(B−V) and $A_{\rm V}$, the opacity to photons that dissociate CO is the real relevant quantity.

3.2. *An Aggregate $I_{\rm CO}-A_{\rm V}$ Relation for Local Clouds*

A main goal of this study is to characterize the typical CO intensity at a given $A_{\rm V}$ and the associated scatter in a typical Solar Neighborhood molecular cloud. That is, we aim to synthesize a typical $I_{\rm CO}-A_{\rm V}$ relationship. To do this, we combine results for our full sample using two different weighting schemes. First, we equally weight each molecular cloud, then we equally weight each individual line of sight.

Figure 3 shows this synthesis. The left panel plots $I_{\rm CO}$ as a function of $A_{\rm V}$, combining measurements of the $I_{\rm CO}-A_{\rm V}$ relation for individual clouds. Here, the cloud-averaged Milky Way $I_{\rm CO}-A_{\rm V}$ relation (shown as green circles with scatter indicated by the error bars) is

TABLE 3
I_{CO} at a Given A_V for the Whole Sample

A_V (mag)	I_{CO} (L.o.S.) (K km s^{-1})	I_{CO} (bins) (K km s^{-1})
0.25	0.3 ± 1.2	0.7 ± 0.6
0.50	1.1 ± 1.5	1.3 ± 1.1
0.75	2.0 ± 2.0	2.3 ± 1.4
1.00	2.9 ± 2.5	3.4 ± 1.5
1.25	3.8 ± 3.1	4.3 ± 2.3
1.50	4.8 ± 3.7	5.1 ± 2.7
1.75	5.7 ± 4.1	6.4 ± 2.4
2.00	7.1 ± 4.4	7.7 ± 2.8
2.25	8.1 ± 4.4	8.6 ± 2.1
2.50	9.3 ± 4.5	9.6 ± 2.4
2.75	10.6 ± 4.4	10.8 ± 2.9
3.00	11.4 ± 4.4	11.8 ± 3.6
3.25	12.5 ± 4.7	12.9 ± 4.2
3.50	13.1 ± 5.0	13.8 ± 4.0
3.75	14.5 ± 4.9	14.8 ± 4.3
4.00	15.4 ± 5.5	15.4 ± 4.7
4.25	15.9 ± 5.0	16.3 ± 4.4
4.50	16.1 ± 5.1	16.8 ± 6.3
4.75	17.0 ± 5.2	17.4 ± 5.4
5.00	18.5 ± 5.1	19.5 ± 3.6
5.25	18.3 ± 5.5	19.2 ± 3.8
5.50	18.7 ± 5.1	18.0 ± 4.1
5.75	21.6 ± 6.6	23.0 ± 5.9
6.00	20.4 ± 5.9	···
6.25	22.2 ± 6.8	···
6.50	22.3 ± 6.7	24.4 ± 9.5
6.75	22.7 ± 8.1	···
7.00	22.6 ± 7.9	···
7.25	23.8 ± 4.6	···
7.50	23.9 ± 5.2	···
7.75	26.8 ± 7.2	···
8.00	24.0 ± 6.8	···
8.25	24.9 ± 6.5	···
8.50	27.4 ± 6.9	···
8.75	30.7 ± 12.0	···
9.00	25.5 ± 10.5	···
9.25	30.7 ± 10.1	···
9.50	28.9 ± 6.9	···
9.75	30.5 ± 7.4	···
10.00	29.4 ± 7.8	···
10.25	33.6 ± 17.1	···
10.50	29.1 ± 16.3	···
10.75	27.6 ± 10.4	···
11.00	33.7 ± 18.9	···
11.25	35.2 ± 13.1	···
11.50	32.7 ± 8.8	···
11.75	34.5 ± 14.5	···
12.00	32.0 ± 16.3	···
12.25	28.4 ± 15.2	···
12.50	32.4 ± 7.3	···
12.75	44.8 ± 9.8	···
13.00	32.2 ± 18.1	···
13.25	33.6 ± 11.3	···
13.50	···	···
13.75	41.4 ± 8.5	···
14.00	···	···
14.25	···	···
14.50	33.8 ± 4.6	···
14.75	···	···
15.00	36.0 ± 11.8	···

Note. — Mean and scatter of I_{CO} in 0.25 mag wide bins of A_V estimated from τ_{850}. L.o.S.: averaging all lines of sight. Bins: averaging binned profiles for individual clouds. We report results for bins with at least 6 data points.

calculated by averaging the binned $I_{CO}-A_V$ profiles of individual clouds. This gives each cloud equal weight and prevents the few clouds with large angular extent from dominating the result. The right panel shows the complementary result. Here, we give all lines of sight across our sample equal weight. In both panels, but especially the right one (equally weighting all lines of sight), the large density of data points in the bottom left corner illustrates that most lines of sight have low A_V and low I_{CO}.

The two weighting schemes result in similar I_{CO} for a given A_V bin, which lends confidence to the generality of our result. Both methods suggest that averaged over our sample, I_{CO} increases close to linearly with increasing A_V in the low-to-intermediate A_V regime ($A_V \leq 4$ mag). As A_V increases further ($A_V \geq 4$ mag), the slope of the $I_{CO}-A_V$ relation becomes shallower. This provides some suggestion of the saturation of CO emission due to high optical depth at high A_V, though not strong evidence. Evidence for a minimum A_V threshold for CO emission ($A_{V,\,thres}$) is even weaker in the aggregate relations, while this feature is predicted by theoretical PDR models and numerical simulations of molecular clouds (Wolfire et al. 2010; Glover & Mac Low 2011). We return to these features in detail below.

4. DISCUSSION

Our average $I_{CO}-A_V$ relationship (Figure 3) and those for individual clouds (see Appendix) highlight that I_{CO} for a given A_V is similar across our sample (see also Table 2). If we compare our results with previous measurements, we find that the Perseus results of Pineda et al. (2008) form an upper envelope for our data, while our average $I_{CO}-A_V$ relation tracks the Lombardi et al. (2006) result for the Pipe Nebula below $A_V \sim 5$ mag. Our results also echo the findings of some of the earliest CO studies, which compared dust extinction to CO emission in nearby molecular clouds (e.g., Dickman 1978; Liszt 1982; Young & Scoville 1982). For instance, Young & Scoville (1982) find similar CO intensity for a fixed A_V in infrared dark clouds and giant molecular clouds in the Galaxy, $I_{CO}/A_V \approx 2.35$ K km s^{-1} mag^{-1} (see Table 6 in the Appendix of their paper), using dust extinction and cloud virial mass estimates to compare with CO intensities. Qualitatively, the good match between dust and CO emission reinforces the idea that shielding by dust plays the primary role in defining the location of bright CO emission within molecular clouds (Wolfire et al. 2010; Glover & Mac Low 2011).

In detail, a number of questions remain: is the normalization of our measurement consistent with expectations? How should we understand the weakness or absence of the expected threshold and saturation features? Are our results consistent with numerical simulations and observations of other galaxies? And if our measured pc-scale relation is universal, what are the implications for the metallicity dependence of the CO-to-H_2 conversion factor? In this section we address each of these topics.

4.1. *Recasting the $I_{CO}-A_V$ Relation in Terms of the CO-to-H_2 Conversion Factor*

Dust and gas are often well mixed in the ISM, so that an approach similar to what we present here has been

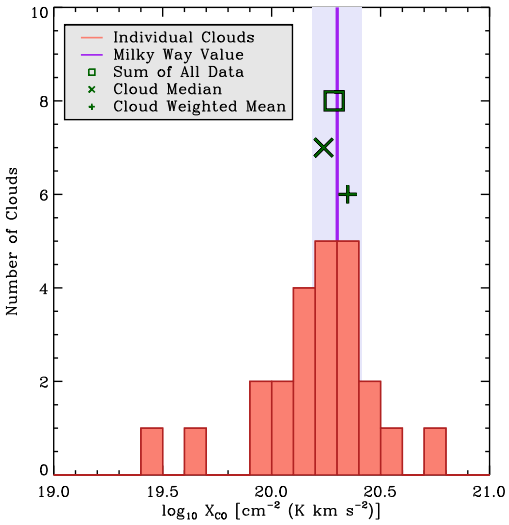

FIG. 4.— The histogram of implied CO-to-H_2 conversion factors in our sample Galactic molecular clouds from the *Planck* dust and CO maps. The histogram plots one value for each cloud. The purple line and shaded region show the recommended Milky Way value of $2{\times}10^{20}$ cm^{-2} (K km s^{-1})$^{-1}$ with a $\pm$30% uncertainty from Bolatto et al. (2013). The green points show different average values derived from our data assuming a standard dust-to-gas ratio and an HI shielding layer of 0.2 mag. The median of all cloud values, a mass-weighted mean, and a calculation weighting each line of sight equally all yield values close to the nominal Galactic value. This close agreement between the two offers a sanity check on our measured $I_{\rm CO}{-}A_{\rm V}$ relation.

used to study the CO-to-H_2 conversion factor directly by comparing the column density of gas implied by dust to the integrated CO intensity. Though we are primarily interested in the actual relationship between $I_{\rm CO}$ and $A_{\rm V}$, recasting our results in terms of the implied $X_{\rm CO}$ factor offers a useful check on the normalization of our results. We do so following the equation below:

$$X_{\rm CO} = \frac{N({\rm H_2})}{I_{\rm CO}} = \frac{\frac{N_{\rm H}}{A_{\rm V}}(A_{\rm V} - 2A_{\rm V}^{\rm HI})}{2I_{\rm CO}} \ . \qquad (1)$$

Here $N_{\rm H}$ refers to the total column density of hydrogen atoms in either the atomic or molecular phase. $A_{\rm V}^{\rm HI}$ is the visual extinction into a cloud where the dominant gas phase transitions from HI to H_2 (see Sternberg et al. 2014). The factor of 2 in front of $A_{\rm V}^{\rm HI}$ accounts for the fact that our $A_{\rm V}$ from dust emission probes the entire line of sight, and so includes the HI shielding layer on both the front and the back side of the cloud. The ratio of total hydrogen column density to visual extinction, $N_{\rm H}/A_{\rm V}$, is observed to be 1.87×10^{21} cm^{-2} mag^{-1} in diffuse Milky Way lines of sight (Bohlin et al. 1978).

Following Eq. 1, if $A_{\rm V}^{\rm HI} = 0$ then a constant $X_{\rm CO}$ factor would appear as a straight line in the $I_{\rm CO}{-}A_{\rm V}$ space. With a finite but small $A_{\rm V}^{\rm HI}$, the curve describing a fixed conversion factor has $I_{\rm CO} = 0$ below $A_{\rm V}^{\rm HI}$, rises quickly, then asymptotes to a straight line. The purple lines in Figure 3 shows the standard $X_{\rm CO}$ in the Milky Way ($2{\times}10^{20}$ cm^{-2} (K km s^{-1})$^{-1}$, Bolatto et al. 2013) for the Bohlin et al. (1978) $N_{\rm H}/A_{\rm V}$ ratio and neglecting $A_{\rm V}^{\rm HI}$. Our data exhibit a slightly shallower slope than this fiducial line (which has a slope of 4.7 K km s^{-1} mag^{-1}), suggesting a slightly higher $X_{\rm CO}$ in our sample.

We also directly calculate the implied $X_{\rm CO}$ for individual clouds from the maps of $A_{\rm V}$ and $I_{\rm CO}$ and Eq. 1. Again, we adopt the Bohlin et al. (1978) $N_{\rm H}/A_{\rm V}$, and now assume that the transition from HI to H_2 takes place approximately at $A_{\rm V}^{\rm HI} = 0.2$ mag for a fixed radiation field (Draine 1978), as motivated by Krumholz et al. (2009); Sternberg et al. (2014).

Figure 4 shows the resulting distribution of $X_{\rm CO}$ values for our sample of local molecular clouds. The median value treating each cloud as one measurement is $X_{\rm CO} \approx 10^{20.2}$ cm^{-2} (K km s^{-1})$^{-1}$ and the cloud-to-cloud scatter is $\sim$0.2 dex, though with a few significant outliers. If we instead weight each cloud by its mass, to derive a weighted Solar Neighborhood value, we find a mean $X_{\rm CO} \approx 10^{20.3}$ cm^{-2} (K km s^{-1})$^{-1}$, while summing over all of our data to derive a single value, we find $X_{\rm CO} \approx 10^{20.35}$ cm^{-2} (K km s^{-1})$^{-1}$.

All of our estimates agree well with the standard Galactic value, which may not be surprising given that this value is partially based on *Planck* and other dust results. Bearing in mind that we expect some departures from the assumed fixed $N_{\rm H}/A_{\rm V}$ and $A_{\rm V}^{\rm HI}$, our $I_{\rm CO}{-}A_{\rm V}$ results appear consistent with the literature on the CO-to-H_2 conversion factor. This provides an important sanity check on our overall measurement.

4.2. *Shape of the $I_{\rm CO}{-}A_{\rm V}$ Relation*

On theoretical grounds, one would expect to observe several features in a highly resolved $I_{\rm CO}{-}A_{\rm V}$ relation. These should reflect the physics of CO emission from PDRs.

First, one would expect to see a threshold visual extinction, $A_{\rm V,\,thres}$, below which the CO emission drops rapidly due to photodissociation of CO molecules (van Dishoeck & Black 1988; Visser et al. 2009). Physically, this reflects the transition of the dominant carbon reservoir from CII in the poorly shielded outskirts of clouds to CO in the well-shielded interiors (e.g. Tielens & Hollenbach 1985). Outside this transition, in regions where most carbon is C and CII, gas and dust still exist, but they lack abundant CO molecules. Thus, we expect the emissivity of gas in CO to be much lower in the outer parts of clouds. This CII-to-CO transition is associated with a particular amount of shielding (see Wolfire et al. 2010). Assuming that the line-of-sight dust column traces the shielding of the gas, then we would expect a drop in $I_{\rm CO}$-per-A_V below some $A_{V,\,thres}$. Recent theoretical models estimate a threshold for bright CO emission to be $A_{\rm V,\,thres} \sim 1{-}2$ mag (e.g. Wolfire et al. 2010; Glover & Mac Low 2011; Glover & Clark 2012b).

One does not truly expect to find no CO below this threshold, as UV absorption studies find both H_2 and CO down to very low column densities (e.g., Sheffer et al. 2008). However, at very low columns, the abundance of CO relative to H_2 does drop steeply. For example, Sheffer et al. (2008) find $N({\rm CO}) \propto N({\rm H_2})^3$ at modest column densities, demonstrating that indeed much less of the C is included in CO at low column densities in the outskirts of clouds. This phenomenon should manifest as a much steeper slope in the $I_{\rm CO}$-A_V relation below $A_{V,\,thresh}$, leading to very low $I_{\rm CO} - to - A_V$ ratios in this regime. There is evidence for this threshold extinction from CO observations of nearby Galactic molecular clouds (Pineda et al. 2008, 2010), though observations of

CO-bright diffuse regions (e.g., Liszt & Pety 2012) suggest that this simple picture does not capture all of the relevant physics. Beyond the classic PDR models mentioned above, the effect is also evident in high physical resolution simulations, such as the one by Glover & Clark (2016) that we compare to below.

One also expects a saturation of $I_{\rm CO}$ at high $A_{\rm V}$ as CO emission becomes optically thick (e.g, Shetty et al. 2011) and CO intensity approaches a constant value regardless of gas column. This effect is expected theoretically. For example, the PDFs of integrated CO intensity in turbulent molecular cloud simulations show a 'piled-up' feature at some high $I_{\rm CO}$ intensity (Shetty et al. 2011; Glover & Clark 2012a). It is also observed, with the best-fit relations for the nearby Pipe Nebula and Perseus molecular cloud showing a saturation of $I_{\rm CO}$ at $A_{\rm V} \geq 10$ mag (e.g., see Figure 3).

The presence or absence of these features have important consequences for the dependence of $X_{\rm CO}$ on metallicity. As we will see in Section 4.4, the $A_{\rm V}$ threshold plays a crucial role in predicting how $X_{\rm CO}$ behaves in low metallicity environments. That can be easily understood in terms of the approach introduced in Lee et al. (2015): for a fixed gas column density PDF, low metallicity (and so a low dust abundance) will shift large amounts of material to have low $A_{\rm V}$. If CO emission is (almost) totally suppressed in this regime then $X_{\rm CO}$ depends strongly on metallicity. The theoretical work by Wolfire et al. (2010) and Glover & Mac Low (2011) both show strong $A_{\rm V}$ thresholds and consequently strong dependence of $X_{\rm CO}$ on metallicity.

4.2.1. *Observed Threshold and Saturation Features*

Do we see a clear threshold and saturation behavior in our data? As discussed above (Section 3.1), both the synthesized $I_{\rm CO}-A_{\rm V}$ relationship and the relations of individual clouds show mixed results. There are some cases where we can visually identify these features. Chamaeleon, the Gum Nebula, Hercules, Lupus, Orion A, and R Coronae Australis show some evidence for a minimum threshold in $A_{\rm V}$ for CO emission. Chamaeleon, Hercules, Lupus, Orion A, the Pipe Nebula, and Taurus show the saturation behavior. When present, the $A_{\rm V,\,thres}$ lies at 0−1 mag, while the CO saturation starts at a large range of $A_{\rm V}$ around 2−5 mag with large variations between clouds.

If a cloud shows one of the features, it is likely to have the other feature as well, and most of the clouds with clear features are the closer members of our sample (within 200 pc), with the exception of the Gum Nebula and Orion A. This strongly suggests that the spatial resolution plays a major role in our ability to detect these features in the $I_{\rm CO}-A_{\rm V}$ relationship. That is, blending of distinct regions by a large beam appears to remove our ability to cleanly isolate poorly shielded regions, and perhaps also heavily shielded regions. Achieving a physical resolution of $\lesssim$ 1 pc seems to be a necessary condition to be able to visually identify the minimum $A_{\rm V}$ threshold for CO emission or the saturation of $I_{\rm CO}$ at high $A_{\rm V}$. Reinforcing this view, we note that we do not find conclusive evidence for these features in the Pipe Nebula and Perseus molecular cloud, where the spatial resolution of the data is 0.7 pc and 1.3 pc, respectively. Previous studies of these clouds (Lombardi et al. 2006; Pineda et al. 2008) using sub-parsec resolution data did find evidence for a threshold behavior in Perseus and saturation in both clouds. We explore the effect of resolution on the $I_{\rm CO}-A_{\rm V}$ relation in a more quantitative fashion in Section 4.2.3.

Factors other than the spatial resolution also contribute to the observed shape of the $I_{\rm CO}-A_{\rm V}$ relation. Some nearby clouds do not show these features even though the spatial resolution should be good enough to identify them. There are also distant clouds with large $A_{\rm V}$ that should show the saturation behavior. Regardless of sub-beam clumping, a beam with average $A_{\rm V} \approx 10$ mag must have a large part of the mass well shielded. However, $I_{\rm CO}$ continues to increase as a function of $A_{\rm V}$ in those clouds.

The accuracy of our estimate of the foreground and background contamination also matters critically to the presence or absence of a threshold. As we noted in Section 2.3, it is notoriously difficult to determine the correct value for the $A_{\rm V}$ that is not associated with the clouds. Recent studies of the column density distribution of Galactic molecular clouds (Lombardi et al. 2015; Schneider et al. 2015) consider the low end of the column density PDF to be highly unreliable due to the ambiguity in the estimation of material unrelated to the cloud, often citing $A_{\rm V} \lesssim 1$ mag as the limiting regime. Unfortunately, this is exactly the regime where any $A_{\rm V}$ threshold for CO emission should emerge. Realistically, because of limited resolution and this uncertainty in the $A_{\rm V}$ zero point, our results place only a weak constraint on the presence or absence of an $A_{\rm V}$ threshold for CO emission. Even in the case where we find circumstantial evidence for $A_{\rm V,thres}$ by eye, we caution that its value is likely very uncertain.

As for the case of the CO saturation at high $A_{\rm V}$, the non-detections of such features may arise from a variation of physical conditions inside the molecular clouds such as gas temperature, turbulent line width, CO opacity, and cloud geometry. In Perseus, Pineda et al. (2008) observe a significant variation of parameters that describe $I_{\rm CO}$ as a function of $A_{\rm V}$ even within this single cloud complex. The clouds missing such features may exhibit similar variations, making the observed CO intensities for high $A_{\rm V}$ lines of sight strongly variable. In this case, averaging many lines of sight may not converge to a constant CO intensity; though, we would still expect a shallower slope at high $A_{\rm V}$.

Finally, we note that not all of our target clouds have enough area that we would expect a large amount of mass at the high $A_{\rm V}$ values needed for the CO saturation. In other words, the combination of low cloud mass and coarse resolution means that we may lose the dense parts of the cloud within a few individual pixels. The notable candidates for this effect are Aquila South, Camelopardalis, Lacerta, Pegasus, and the Polaris Flare.

4.2.2. *Comparison to Theoretical Work*

Both photon dominated region models (Wolfire et al. 2010) and numerical simulations (e.g. Glover & Mac Low 2011) identify the dust extinction ($A_{\rm V}$) as the key parameter for the location of CO in a molecular cloud. Our observational study of the $I_{\rm CO}-A_{\rm V}$ relationship in Milky Way molecular clouds is directly motivated by these previous works. Here, we make a direct comparison between

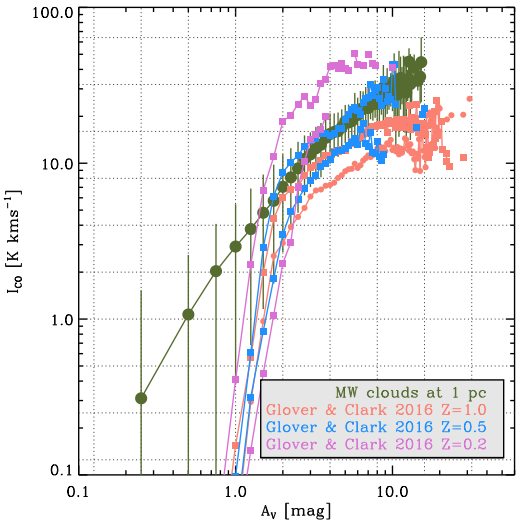

FIG. 5.— Comparison of our synthesized Milky Way $I_{CO}-A_V$ relationship with theoretical expectations. Our $I_{CO}-A_V$ relation weighting all lines of sight equally appears in green with error bars showing the scatter. Points show the $I_{CO}-A_V$ relations for three different metallicity clouds (i.e., 1, 0.5, 0.2 solar metallicity) with fixed mass (10^4 $M_\odot$) and radiation field (Draine 1978) from the simulations by Glover & Clark (2016). For each cloud, we plot the simulation at two times: at the onset of star formation (the upper line) and 1 Myr before this time (the lower line). The theoretical $I_{CO}-A_V$ relations show some dependence on metallicity, with higher CO emission at a given A_V in lower metallicity systems. At intermediate $A_V \approx 2-5$ mag, our measurements agree well with the star-forming Solar metallicity clouds and both $Z = 0.5$ clouds, and lie between the star-forming low metallicity and inert high metallicity cloud. All of the simulations show clear signatures of a minimum A_V threshold for CO emission and saturation of the CO line at high A_V. Such a features are not obvious in the observations, at least partially due to the lack of resolution.

the results of our observations and theoretical predictions.

Specifically, we compare our observational results to the recent simulations by Glover & Clark (2016). They used a modified version of the Gadget 2 SPH code (Springel 2005) to simulate molecular clouds with different initial conditions. We consider runs with three different metallicities: 1.0, 0.5, and 0.2 solar metallicity ($Z_\odot$). They assumed that the dust-to-gas ratio scales linearly with metallicity. All three runs assume the same standard Draine (1978) UV radiation field, a fixed cosmic ray ionization rate of 10^{-17} s^{-1} per hydrogen atom. The cloud mass is 10^4 $M_\odot$ and the initial volume density is 276 cm^{-3}. The initial turbulent velocity field is the same and chosen such that the cloud is initially marginally gravitationally bound (i.e., the initial kinetic energy is the same as the gravitational binding energy of the cloud). The turbulence is decaying over time, and the simulations are evaluated at two times: at the initial onset of star formation and 1 Myr before this time. This set of simulations corresponds to placing a low-mass Galactic cloud into environments with metallicities similar to the Milky Way (1.0 $Z_\odot$), the LMC (0.5 $Z_\odot$), and the SMC (0.2 $Z_\odot$).

Glover & Clark (2016) generate integrated CO intensity maps from the underlying SPH simulations using RADMC-3D[9]. They used the large velocity gradient (LVG) approximation to calculate the level populations of CO molecules, as described in Shetty et al. (2011). The size of the final A_V and CO maps from the simulations is 16.2 pc per side, and the number of pixels is 256^2 (making a pixel ∼0.06 pc big). The spatial resolution of the simulated maps is thus comparable to extinction maps of nearby clouds (Lombardi et al. 2006; Pineda et al. 2008) and a factor of few higher than the data that we use in this paper.

Figure 5 compares our observed $I_{CO}-A_V$ relation (the green circles and error bars showing the 1σ scatter) to the simulation results. At intermediate $A_V \approx 2-5$ mag, the simulation at half solar metallicity most closely resembles our observed relation, though the solar metallicity calculation at the onset of star formation shows only a small offset towards lower I_{CO} at fixed A_V compared to our measurements. We will see below that this intermediate range appears least affected by resolution effects.

The simulations exhibit strong evidence for a minimum A_V threshold for CO emission. They show a steep drop in CO emission as A_V approaches ∼1 mag, reflecting the need for a dust layer to shield CO molecules from dissociating radiation. On the other hand, the observations produce a smooth relationship between CO and A_V at low A_V. Following on the previous section, we highlight uncertainty in the contamination correction and the high spatial resolution of the simulation, ∼0.2 pc, compared to our $\gtrsim$ 1 pc beam. We demonstrate the impact of resolution by blurring the simulation in the next section.

The saturation of CO emission at high A_V is also apparent in the simulations, consistent with the results found in Shetty et al. (2011). Our average $I_{CO}-A_V$ relation shows some hint of saturation when plotted in linear scale (Figure 3), but this plot shows that any such effect remains weak compared to the same behavior at high resolution in the simulations. Again, we expect resolution to play an important role, but it cannot explain the whole difference. Variations among the properties of clouds in our sample must also contribute to the observations, such that any saturation sets in at even higher A_V for our highest mass clouds.

In Section 4.3 we compare our results to those found for the Magellanic Clouds by Lee et al. (2015). With that in mind, we highlight the differences among the Glover & Clark (2016) results for clouds of different metallicities. In the simulations, a molecular cloud with a lower metallicity but otherwise identical initial physical conditions shows stronger integrated CO intensity at a given A_V compared to a higher metallicity cloud. Plotting the data in this way attempts to control for dust shielding and the simulations fix the strength of impinging radiation field. Therefore, the difference seems most easily attributed to differences in CO excitation. Key to this paper, this sorting by metallicity contrasts with the observation by Lee et al. (2015) who find similar CO emission at a given A_V in three different metallicity galaxies (the Magellanic Clouds and the Milky Way) at 10 pc resolution.

4.2.3. *Effect of Spatial Resolution*

[9] http://www.ita.uni-heidelberg.de/~dullemond/software/radmc-3d/

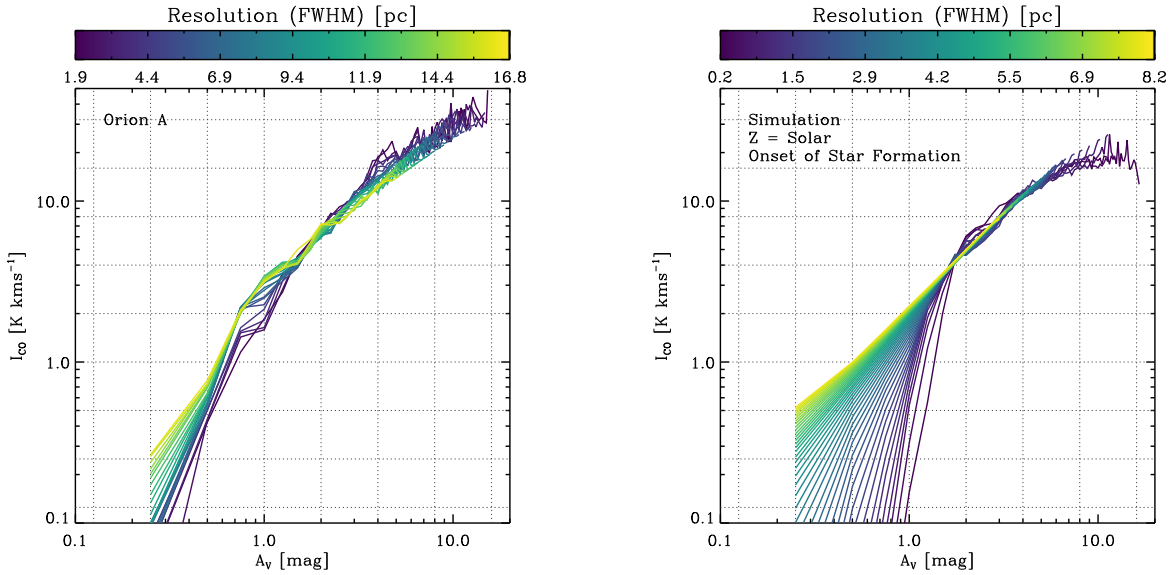

FIG. 6.— Effect of spatial resolution on the $I_{CO}-A_V$ relation. (*left*) I_{CO} as a function of A_V in the Orion A molecular cloud measured at different resolutions. We progressively degrade the resolution to simulate observing a more distant cloud and plot the mean relation colored according to the resolution of the data. (*right*): A similar exercise using the Glover & Clark (2016) simulations of a Solar metallicity cloud at the onset of star formation. In both cases, the dynamic range in the $I_{CO}-A_V$ relation is reduced as the spatial resolution becomes progressively coarser. As the resolution changes, I_{CO} at a given A_V does not vary much in the intermediate A_V regime, but at high and low A_V the situation is different. Any threshold and saturation are washed out as the convolution blurs together intermediate A_V gas and either high or low A_V gas. This makes the threshold and saturation effects hard or impossible to measure at coarse spatial resolution. Based on the simulation data, ∼0.1 pc may be a useful figure of merit.

We argue that our ability to detect an A_V threshold for CO emission or the saturation of CO intensity at high A_V can be significantly diminished by insufficient spatial resolution. The high resolution of the Glover & Clark (2016) simulations allows us to test this hypothesis. The simulations show threshold and saturation features at their native resolution of ∼0.1 pc. To test whether these features could be recovered at coarser spatial resolution, we blur the I_{CO} and A_V maps from their solar metallicity cloud simulation. We convolve these data with progressively larger and larger kernels and then measure the $I_{CO}-A_V$ relation at ever coarser resolution. We perform the same test on the data for the Orion A molecular cloud, which is relatively nearby and shows some hint of an A_V threshold and I_{CO} saturation (see Figure 20).

Figure 6 shows the results of this test. For both the real and simulated cloud, the slope of the $I_{CO}-A_V$ relation at low A_V tends to become shallower as the spatial resolution becomes coarser. At $A_V \leq 1$ mag the mean CO intensity at a given A_V become systematically higher for the lower resolution data. The effect is stunningly strong in the simulation, with the threshold all but vanishing by the time we degrade the resolution to a few pc (though we do caution that at these scales, the resolution begins to approach the scale of the whole simulated cloud). The apparent A_V threshold for CO emission shifts to lower A_V or vanishes as the resolution of our data becomes worse. At the same time, the dynamic range in A_V is significantly reduced as we degrade the spatial resolution. As the maximum A_V becomes smaller, the saturation behavior of I_{CO} at high A_V becomes progressively harder to identify.

These tests have important implications for our results. First, note that the I_{CO} at intermediate A_V (i.e., a few mag) appears reasonably robust to resolution effects. As a result, this normalization should be viewed as our main, most secure result and, indeed, one of our main goals was to compare this value among clouds and to other galaxies. Second, we will see below that the threshold behavior is crucial for the metallicity dependence of X_{CO}. To constrain this with observations, one needs high (significantly sub-parsec) resolution data, beyond the reach of the *Planck* data. The "blurring" along the A_V axis induced by changing resolution will also affect the PDF, so that ideally one also needs to measure or model the A_V distribution at high resolution.

4.3. *Comparison to Other Galaxies*

A main goal of our paper is to extend the work of Lee et al. (2015), who found a similar amount of CO emission at a given A_V using matched spatial resolution (10 pc) data in the Milky Way, the LMC, and the SMC. This similarity across a wide range of metallicity implies that the amount of dust shielding is the primary factor in determining the extent of CO emission, and this idea agrees with theoretical expectations (e.g., Wolfire et al. 2010; Glover & Mac Low 2011) and the results of the recent simulations by Glover & Clark (2016, see above). But in the work by Lee et al. (2015), the available Milky Way data represented the limiting factor allowing only a few cloud-averaged and high latitude lines of sight measurements. Here, we ask how our new results for our large set of local molecular clouds compare to the measurements of the Magellanic Clouds in Lee et al. (2015).

Figure 7 plots this comparison. We show our synthesized Milky Way $I_{CO}-A_V$ relation with measurements at lower resolution from Lee et al. (2015) for the Large Magellanic Cloud (0.5 $Z_\odot$), the Small Magellanic Cloud (0.2 $Z_\odot$), and high latitude ($|b| > 5$ degrees) sight lines in the Milky Way ($Z_\odot$). All these comparison data have

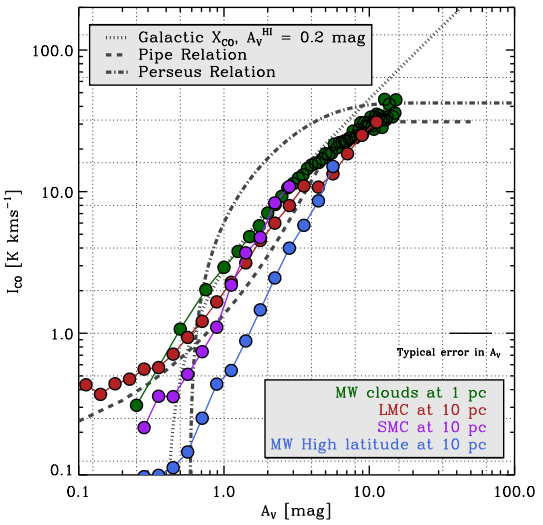

FIG. 7.— Comparison of $I_{CO}-A_V$ relations in Local Group galaxies. The relations for the LMC, SMC, and high latitude Milky Way are taken from Lee et al. (2015), and are measured on 10 parsec scales. The synthesized Milky Way relation plotted here is calculated by weighting all the lines of sight equally (i.e., the right panel in Figure 3) and has resolution of ∼1 parsec at the median distance of 200 parsec. The gray dotted line shows the standard Galactic X_{CO}, assuming that all hydrogen is in molecular phase. The gray dashed line shows the same, but for the case of a fixed HI shielding layer of $A_V^{HI} = 0.2$ mag.

spatial resolution of ∼10 pc, approximately an order of magnitude coarser than our synthesized Milky Way relation. We also plot the curves that are expected for the standard Galactic CO-to-H_2 conversion factor (gray dotted line) and an HI shielding layer of $A_V^{HI} = 0.2$ mag (gray dashed line).

To first order, our synthesized Milky Way, LMC, and SMC relations agree well, especially given the uncertainty in the x-axis. These three galaxies span a factor of ∼5 in metallicity. Their good agreement in this parameter space highlights the central role of dust shielding in determining CO emission. A given amount of dust column on the scale of a cloud predicts the amount of CO emission well, to first order independent of environment. There are fine differences in the $I_{CO}-A_V$ relationship from region to region, of course. These are clear from our atlas of clouds, Pineda et al. (2008) showed them in Perseus, and Lee et al. (2015) demonstrated differences in the $I_{CO}-A_V$ relation between different regions in the LMC when sorted by T_{dust}. Despite these differences, Figure 7 offers good support to the idea that as a practical tool, A_V can be used to predict I_{CO} with reasonable accuracy across systems with different metallicity.

Note that the high latitude Milky Way lines of sight stand out most in this plot, especially at low A_V. These have the lowest CO intensity per unit visual extinction. This behavior was noted by Lee et al. (2015), who attributed the low CO emission per unit visual extinction to the long path length through the thick Galactic atomic gas disk at high latitudes. Most of the gas, and most of the dust, in most lines of sight at $|b| > 5°$ is physically unassociated material spread our over ∼kpc along the line of sight.

Finally, note that with ∼1 pc resolution, we expect the present measurements to be more accurate than the LMC and SMC relations or the cloud-averages in Lee et al. (2015). As we saw above, the better resolution does a better job of not blurring out cloud structure. The higher resolution also allows us to correct for contamination by material unassociated with the clouds. The coarser resolution in the Magellanic clouds prevented such an operation, and we relied on the external line of sight (and lower dust content of contaminating HI) in Lee et al. (2015). Future, higher resolution work, especially with ALMA, will improve the quality of mapping of the Magellanic Clouds and will allow a similar approach to what we use in this paper.

4.4. *Implications for X_{CO} as a Function of Metallicity*

Based on the observation of similar I_{CO} at a given A_V in the LMC, SMC, and Milky Way, Lee et al. (2015) argued that I_{CO} may be reasonably predicted from A_V in an approximately universal way in highly resolved molecular clouds. In this case, they suggest that the dependence of X_{CO} can be modeled as a separable problem with four individually tractable parts:

1. Clouds have some distribution of gas column densities (*the column density PDF*).

2. That distribution of column densities translates to some distribution of dust column densities, expressed as A_V. The gas column relates to the dust column via the *dust-to-gas* ratio, which is a function of metallicity.

3. Below some A_V, most of the gas is atomic. Inside that *atomic shielding layer*, the gas is mostly molecular (H_2).

4. In the molecular gas, the amount of CO emission can be predicted from the line of sight extinction via the $I_{CO}-A_V$ *relation.*

Our findings in Section 3.2 suggest that the fourth step, the prediction of the CO intensity from A_V may be valid to good approximation. Thus this further motivates the empirical approach. Here we revisit and extend the calculations of Lee et al. (2015), also noting future areas for improvement in the calculations and needed observations.

We refer the readers to Lee et al. (2015) for more details on the basic calculation, but summarize the approach here. The starting point of the calculation is a realistic distribution of gas column densities (N_H). In Lee et al. (2015), this is computed from a library of cloud column density PDFs observed in the Milky Way (Kainulainen et al. 2009). In this work, we try a more direct approach instead and consider the observed A_V distribution from the *Planck* map to infer an alternative baseline gas column density PDF for the solar metallicity clouds.

X_{CO} and DGR for the whole sample: First, we work with the full set of lines of sight across our sample and the average $I_{CO}-A_V$ relation derived from them. This renders this exercise approximate, because the clouds are at different distances and in different physical states. But the exercise is still illuminating. We suggest thinking of it as asking how CO emission from an ensemble of Solar

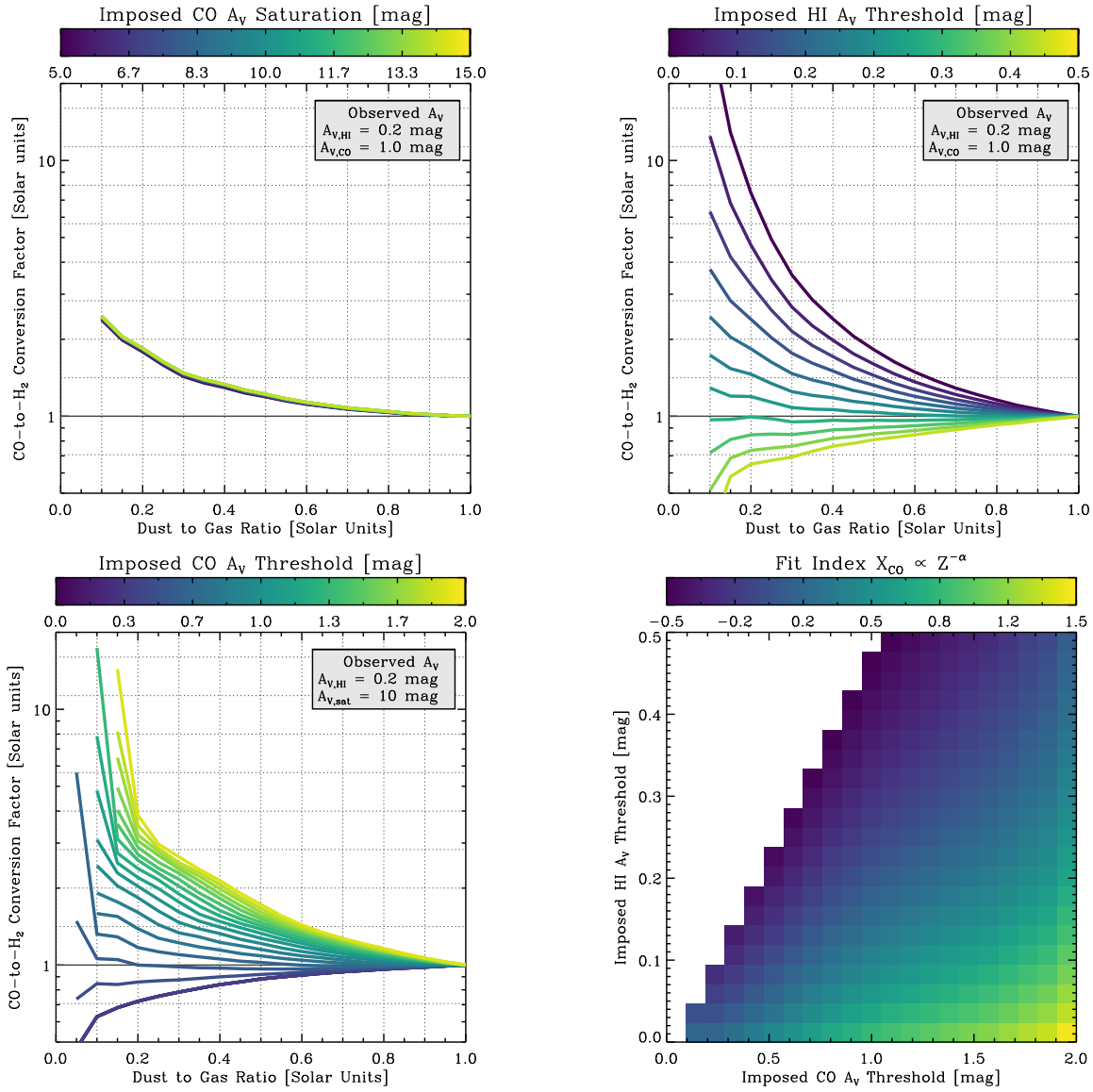

FIG. 8.— The CO-to-H_2 conversion factor as a function of metallicity, following the four-step approach in Lee et al. (2015, see that paper for an illustration). We use a modified version our aggregate $I_{CO}-A_V$ measurement for local molecular clouds, along with the measured distribution of A_V from τ_{850} to explore how X_{CO} would change if we observe an analog of the Solar Neighborhood clouds but at different dust-to-gas ratio. In this approach the dust-to-gas ratio and X_{CO} are both normalized to equal 1 at the value calculated for our maps. The behavior of X_{CO} as a function of DGR pivots on features still below the resolution of our data, and we show the sense of this here. We vary the (*top left*) CO saturation, (*top right*) A_V threshold of the CO-to-H_2 transition, and (*bottom left*) A_V threshold for detectable CO emission. The CO saturation has negligible impact on the metallicity dependence. By contrast, any threshold for CO emission and the thickness of the atomic gas shielding layer both have large impacts. The *bottom right* panel shows the interplay of the CO threshold and HI shielding layer. We plot the best fit power law index, α, in $X_{CO} \propto Z^{-\alpha}$ as a function of the adopted CO-to-H_2 and CO thresholds. We only show results where the CO threshold exceeds twice the HI threshold (in our book-keeping the CO-to-H_2 threshold is one sided and the CO threshold is two sided). The steepest metallicity dependence comes from cases with a large CO-dark layer, i.e., high CO threshold and low CO-to-H_2 transition.

Neighborhood clouds would change if this region were moved to a low metallicity galaxy.

We translate the A_V distribution for the local clouds into a distribution of line of sight dust column densities at a different metallicity by multiplying the gas column density by the dust-to-gas ratio. Following Lee et al. (2015) we assume that the dust-to-gas ratio is directly proportional to metallicity. This calculation provides an estimate of the dust extinction, A_V, distribution for a given molecular cloud PDF at any metallicity.

Next, we label the parts of the A_V PDF below the HI−H_2 threshold as HI and then remove these from the rest of the calculation. Formally, we subtract $2A_V^{HI}$ from all of our predicted A_V values. This accounts for the shielding layer along the line of sight and identifies the well-shielded molecular gas in the clouds. As in Section 4.1, our fiducial HI shielding layer is $A_V^{HI} = 0.2$ mag (Krumholz et al. 2009; Wolfire et al. 2010; Sternberg et al. 2014), but we also test the effect of varying A_V^{HI}.

Finally, from the A_V distribution associated only with molecular gas, we predict the amount of CO emission using an adopted $I_{CO}-A_V$ relation. We use our measured

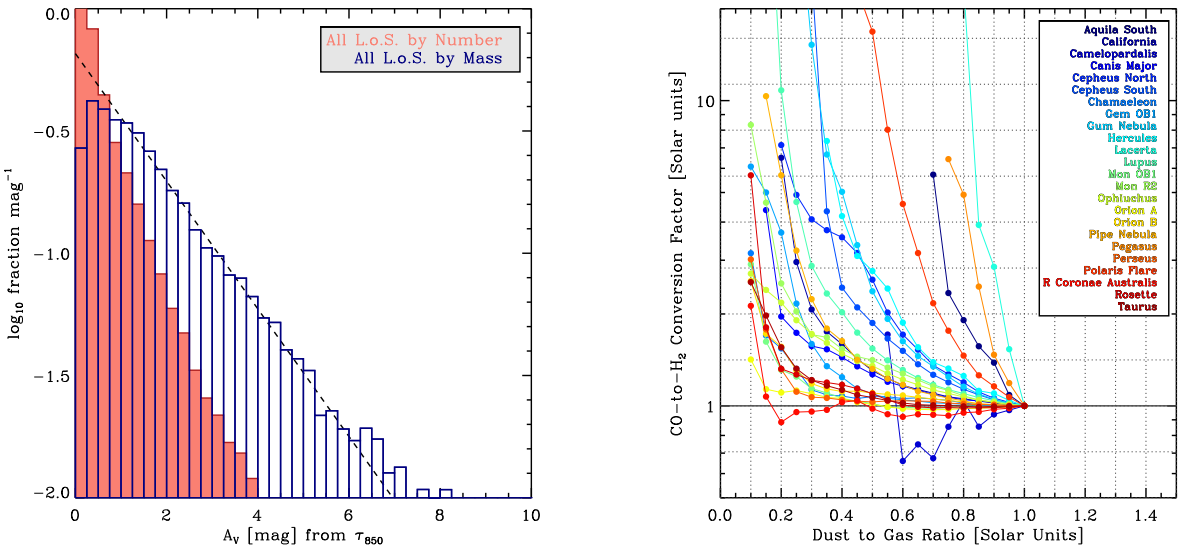

FIG. 9.— (*left*) The distribution of lines of sight (red, filled histogram) and mass ($\propto A_V$, blue, open lines) as a function of A_V for our whole sample. The shape of the combined distribution is self-similar (nearly a power law; the dashed line shows slope −0.26.), contributing to the flat behavior of X_{CO} in Figure 8. (*right*) X_{CO} as a function of dust to gas ratio inferred for individual clouds, assuming a threshold for CO emission of $A_{V,thres} = 1$ mag and an HI shielding layer of 0.2 mag. We observe a large diversity in behavior from cloud-to-cloud, so that X_{CO} can be expected to be a strong function of the cloud column density distribution, properties, and evolutionary state. At any given subsolar metallicity, the plot suggests that we should expect large cloud-to-cloud scatter in X_{CO}.

relation with two modifications: we explore the effect of adding a threshold for CO emission, $A_{V,thres}$ even though we show above that our data have too coarse a resolution to find such a feature. We also explore the effect of implementing a sharp saturation, an A_V above which I_{CO} remains fixed at some value.

By summing the CO emission and the molecular gas column in the model, we calculate a CO-to-H_2 conversion factor for that model cloud. We change the dust-to-gas ratio from ∼0.1 $Z_\odot$ to 1 $Z_\odot$ for each model. Repeating the calculation for many values of the dust-to-gas ratio, we can predict the behavior of X_{CO} versus metallicity (Z) given an input PDF (here the whole Solar Neighborhood ensemble) and the assumptions derived above.

Central Role of the CO Threshold and HI−H_2 *Transition in* X_{CO} *vs DGR:* Figure 8 shows that our adopted A_V^{HI} and $A_{V,thres}$ essentially determine the behavior of X_{CO}. Each panel plots the calculated behavior of X_{CO} (i.e., the ratio of H_2 mass to CO emission) as a function of metallicity for many models. In the top left panel we vary the saturation level for CO while holding the other parameters fixed. This has negligible effect for the metallicity dependence, though these physics can be highly relevant in other regimes (Shetty et al. 2011).

The top right and bottom left panels show X_{CO} as a function of metallicity as we vary the A_V threshold for the atomic-to-molecular transition. The bottom left shows the results of varying the threshold for CO emission, below which we take $I_{CO} = 0$. Both of these quantities dramatically affect the behavior of the conversion factor as a function of metallicity. Over the plausible range of values that we explore the behavior shifts from almost no dependence of X_{CO} on Z to very steep values.

The most basic conclusion from this exercise should be that better statistical constraints on both the threshold for CO emission and the threshold for HI shielding will help this field. Certainly a great deal is already known from absorption work (e.g., Sheffer et al. 2008) and theory (e.g., Wolfire et al. 2010; Sternberg et al. 2014), but we still emphasize that these quantities are pivotal to the behavior of X_{CO}.

In detail, Figure 8 shows that one needs to know both A_V^{HI} and $A_{V,thres}$. The strongest dependence of X_{CO} on DGR occurs in regions with a large threshold for CO emission but a low A_V^{HI}, i.e., in regions with a large "CO-dark" component expressed in units of A_V. This agrees with the detailed models of Wolfire et al. (see 2010).

A plane fit to the parts of the diagram where $A_{V,thres} < 2A_V^{HI}$ yields $\alpha \approx 0.3{+}0.725A_{V,thres}{-}3.0A_V^{HI}$ where $X_{CO} \propto DGR^{-\alpha}$ over the range $DGR = 0.1{-}1.0$. A fit using $\Delta A_V = A_{V,thres} - A_V^{HI}$ can also predict α, but with less precision.

Divergence at very Low DGR and Shallow Metallicity Dependence Above: We see the divergence at metallicity $Z < 0.2$ $Z_\odot$ also noted by Lee et al. (2015). This breakdown occurs over a fairly wide range of assumptions. It reflects that in the Solar Neighborhood, most lines of sight and most mass in molecular gas lies at comparatively low $A_V \lesssim 5$ mag. We show this distribution in the left panel of Figure 9. If we imagine keeping the gas column density distribution but scaling down the DGR, then at $Z \lesssim 0.2$ $Z_\odot$ all of this gas lies at $A_V \lesssim 1$ mag and its behavior becomes highly sensitive to our adopted assumptions. As a result, at even moderately low DGR, one moves into the situation where only a small fraction of the cloud emits strongly in CO (see Glover & Mac Low 2011; Lee et al. 2015, among many others).

At intermediate metallicities ($Z > 0.2$ $Z_\odot$, we find a relatively weak metallicity dependence for X_{CO}. The exact number depends strongly on our assumptions, but often in the range $\alpha \sim 0.5{-}1.5$ in $X_{CO} \propto Z^{-\alpha}$. This range of α is shallower than many previous studies, including Israel (1997); Leroy et al. (2011); Schruba et al. (2012);

Lee et al. (2015), and more similar to the shallower slopes ($\alpha > -1$) often found from analyses based on CO virial masses (Wilson 1995; Rosolowsky et al. 2003; Bolatto et al. 2008). However, those measurements have also been interpreted to apply only to the CO-bright parts of clouds, so we do not expect the comparison to be rigorous.

Again the distribution of A_V and mass explains the relatively weak dependence for X_{CO} in our exercise. As we see from the left panel in Figure 9, our ensemble of measurements shows an approximately power law distribution over the range $A_V \approx 2-6$ mag. This does not necessarily bear on the appropriate general shape of the column density PDF, which has been explored in detail by Kainulainen et al. (2009); Abreu-Vicente et al. (2015); Lombardi et al. (2015). We know that power law tails certainly do exist in some of our clouds (Kainulainen et al. 2009), and these are enough to give the ensemble distribution a self-similar shape. As a result, the ratio of gas above any pair of thresholds will remain relatively fixed. The shape of the $I_{CO}-A_V$ relation and deviations from self-similarity will create the behavior that we observe. By contrast, in a curving distribution like a log-normal, the shape of the PDF can contribute strongly to a steep X_{CO} vs. metallicity dependence.

Strong Cloud-to-Cloud Variations: We also carry out this exercise for each individual cloud. We use our fiducial $A_V^{HI} = 0.2$ mag and a CO threshold $A_{V,thres} = 1$ mag. We plot the results in the right panel of Figure 9. This exercise highlights that we should expect dramatic conversion factor variations from cloud-to-cloud in a low metallicity system. Taking this result at face value, if we shifted the Solar Neighborhood clouds to the metallicity of the SMC, some would appear approximately Galactic in nature, while others would disappear almost entirely, showing little or no CO emission. Here we continue to use our average $I_{CO}-A_V$ relation, so this plot mainly reflects variations in the underlying A_V PDFs of the clouds.

Some evidence of such effects have recently been reported in Schruba et al. (2017), who found suggestions of strong field-to-field conversion factor variations in the Local Group low metallicity galaxy NGC 6822. They suggest that these may relate to either temporal or structural changes related to the star-forming state of a cloud. Simulations of molecular clouds at these metallicities by Glover & Clark (2016) also find evidence for strong temporal variations in the conversion factor.

5. CONCLUSIONS

We measure the parsec scale relationship between I_{CO} and A_V in 24 local Milky Way molecular clouds using *Planck* dust and CO maps (Planck Collaboration et al. 2013a,b). After correcting for contamination along the line of sight, we present measurements for each cloud individually and a combined relation derived from our ensemble of local clouds. These local clouds occupy a common region in the $I_{CO}-A_V$ parameter space, sweeping out a relation that closely resembles that found for the Magellanic Clouds by Lee et al. (2015) at coarser (10 pc) resolution. This agreement across a factor of five in metallicity reinforces the idea that dust shielding (A_V) is the primary determinant of the location of CO emission. Moreover, the observed line of sight dust column can be used to estimate CO emission (I_{CO}) with reasonably good accuracy across environment. We also show that our measured relation agrees well with numerical simulations of CO emission from molecular clouds by Glover & Clark (2016).

Although our measured synthesized relation shows a declining slope, expected sharp features such as a minimum A_V threshold for CO emission or the saturation of I_{CO} at high A_V are weak or absent in the aggregate $I_{CO}-A_V$ relationship and the individual $I_{CO}-A_V$ relation for many clouds. The clouds that do show such features tend to be the closest in our sample. By convolving high resolution observations and simulations, we show that degrading sub-parsec resolution data to coarser values tends to wash out such features and lower the dynamic range in A_V. This, combined with the significant difficulty in estimating line of sight contamination, renders direct observations of the A_V threshold for CO emission challenging. But we also emphasize that quantitative measurements of the value and variation in the A_V threshold for CO emission (and the closely related threshold for the molecular-to-atomic transition) remain absolutely crucial to an accurate estimate of X_{CO} as a function metallicity.

Using the $I_{CO}-A_V$ relations that we observe for Milky Way clouds, we explore the implied metallicity dependence of the CO-to-H_2 conversion factor. Our calculations, based on the empirical approach from Lee et al. (2015) leverage the observed A_V distribution and $I_{CO}-A_V$ relation. A main result of these calculations is that, as one might expect, the dependence of X_{CO} on metallicity pivots on the adopted threshold for CO emission and HI-to-H_2 shielding layer; any CO saturation plays only a small role. These two quantities interact with one another, so that strong variation in X_{CO} as a function of metallicity arise in cases with a large "CO dark" layer. Again, improved observational constraints are key and appear to require spatial resolutions of order 0.1 pc.

Our calculations imply strong cloud-to-cloud variations in how X_{CO} depends on metallicity, so that one should expect strong conversion factor variations across a highly resolved data set studying a low metallicity galaxy. Treating our whole sample together, we tend to find divergence in X_{CO} below $Z \sim 0.2\ Z_\odot$, as only a small part of a Solar Neighborhood cloud remains well-shielded at these metallcities. Above this, we find relatively weak dependence of X_{CO} on DGR. In large part, this reflects the self-similar shape of the A_V distribution in our sample. Power law tails in the column density distribution (e.g., Kainulainen et al. 2009; Schneider et al. 2015; Abreu-Vicente et al. 2015) combine to give our overall sample a power law shape, which minimizes the impact of the PDF on X_{CO} (compared to, say, a pure lognormal shape).

In the near future, we expect similar (∼pc) resolution observations of Local Group dwarf galaxies. The results here are intended to serve as a point of comparison for such studies.

We thank the referee of the paper, Paul Goldsmith, for constructive and encouraging reports that helped improve the paper. We thank the *Planck* team for the public release of the dust and CO maps that form the

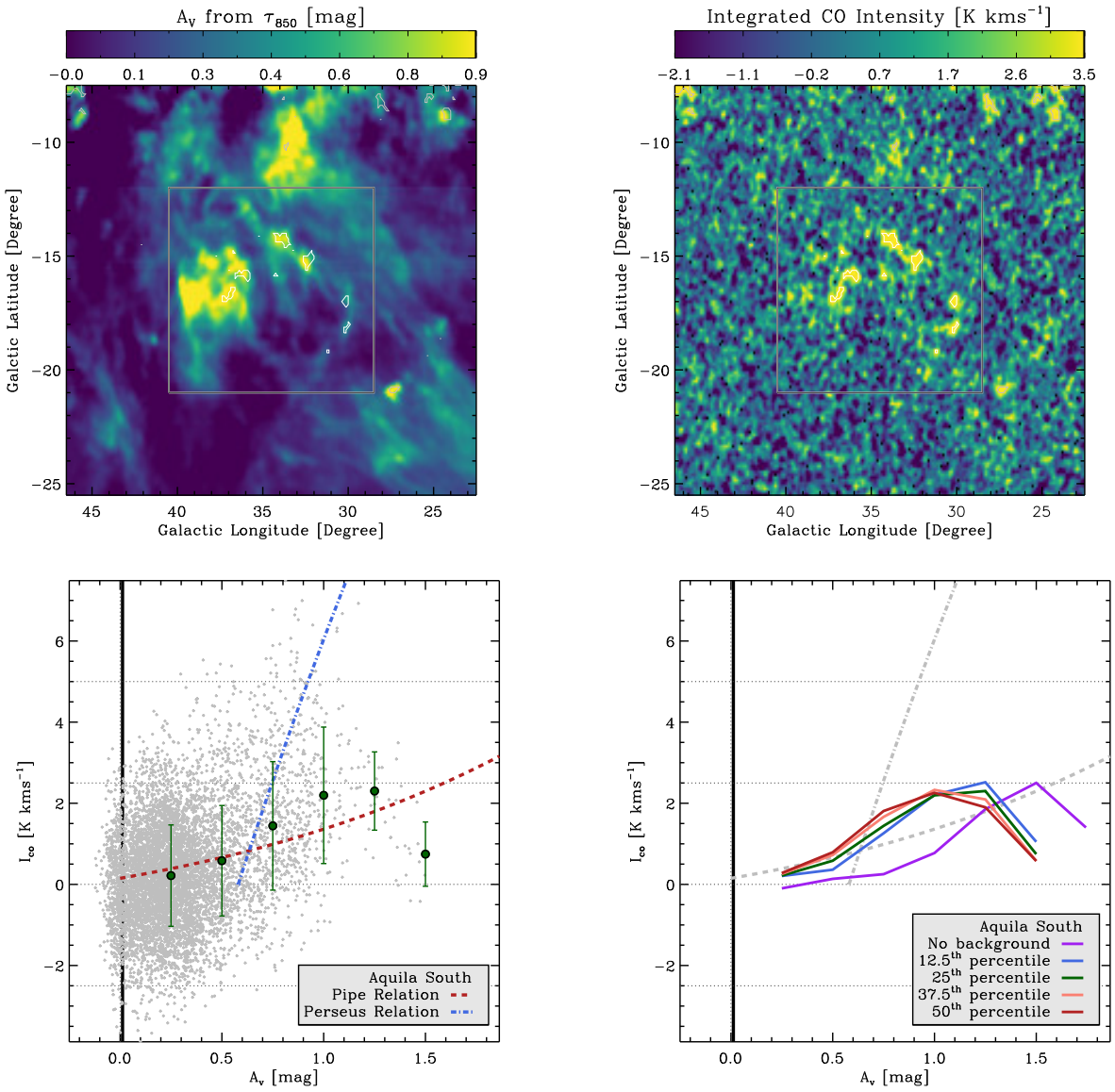

FIG. 10.— Same as Figure 2, for the case of Aquila South.

core of this paper. These are a product of ESA/Planck, the Planck Collaboration, and the papers cited in the main text. During preparation of this paper, support for the work of C. Lee was partially provided by NASA for program HST-GO-12055.027-A through a grant from the Space Telescope Science Institute, which is operated by the Association of Universities for Research in Astronomy, Inc., under NASA contract NAS 5-2655. The work of AKL is partially supported by the National Science Foundation under Grants No. 1615105, 1615109, and 1653300. ADB acknowledges partial support from NSF-AST1412419. SCOG acknowledges financial support from the Deutsche Forschungsgemeinschaft via SFB 881 "The Milky Way System" (sub-projects B1, B2, B8) and SPP 1573 "Physics of the Interstellar Medium" (grant number GL668/2-1), and by the European Research Council under the European Community's Seventh Framework Programme (FP7/2007-2013) via the ERC Advanced Grant STARLIGHT (project number 339177).

APPENDIX

$I_{CO}-A_V$ RELATION FOR INDIVIDUAL MOLECULAR CLOUDS

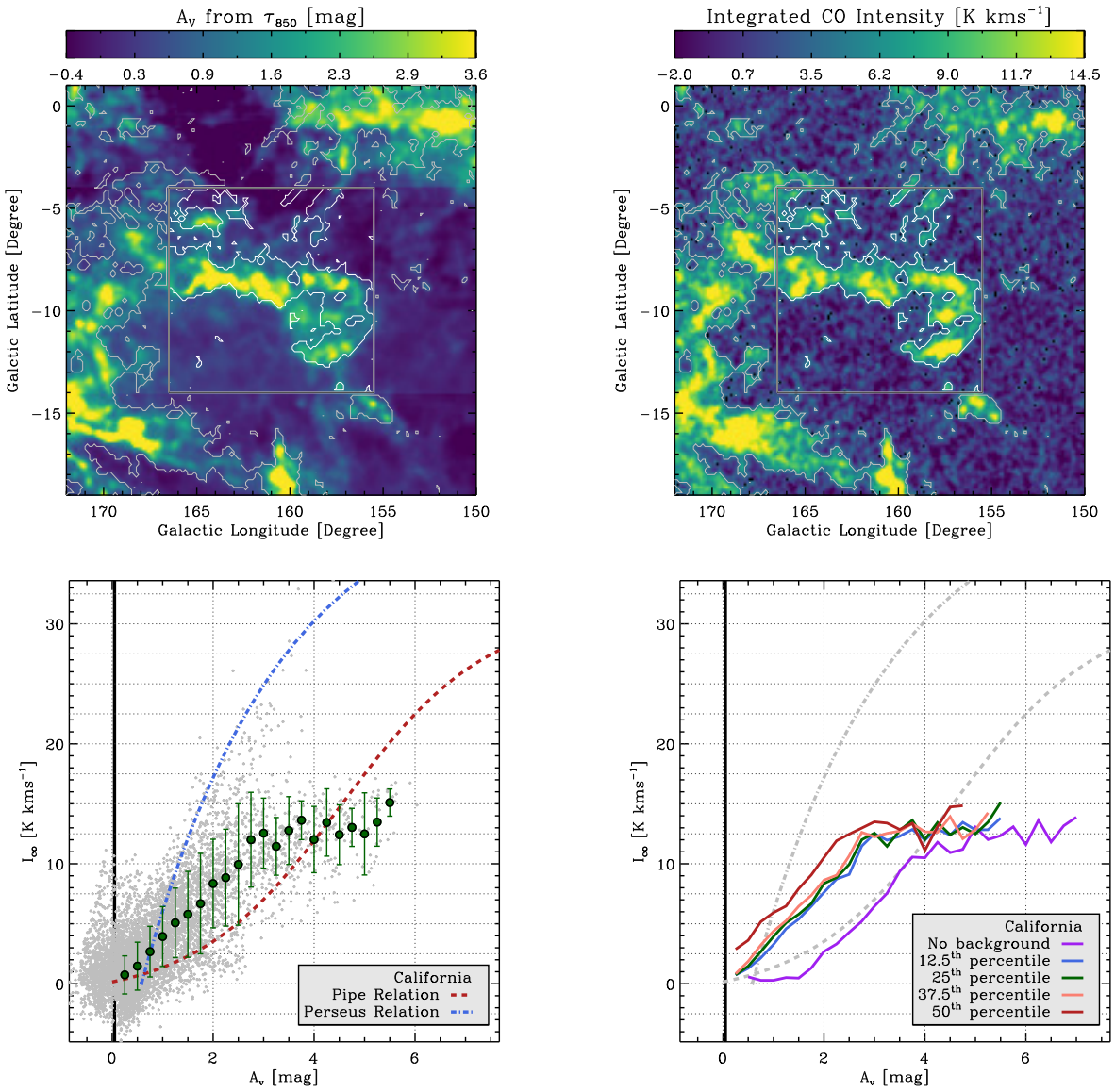

FIG. 11.— Same as Figure 2, for the case of California.

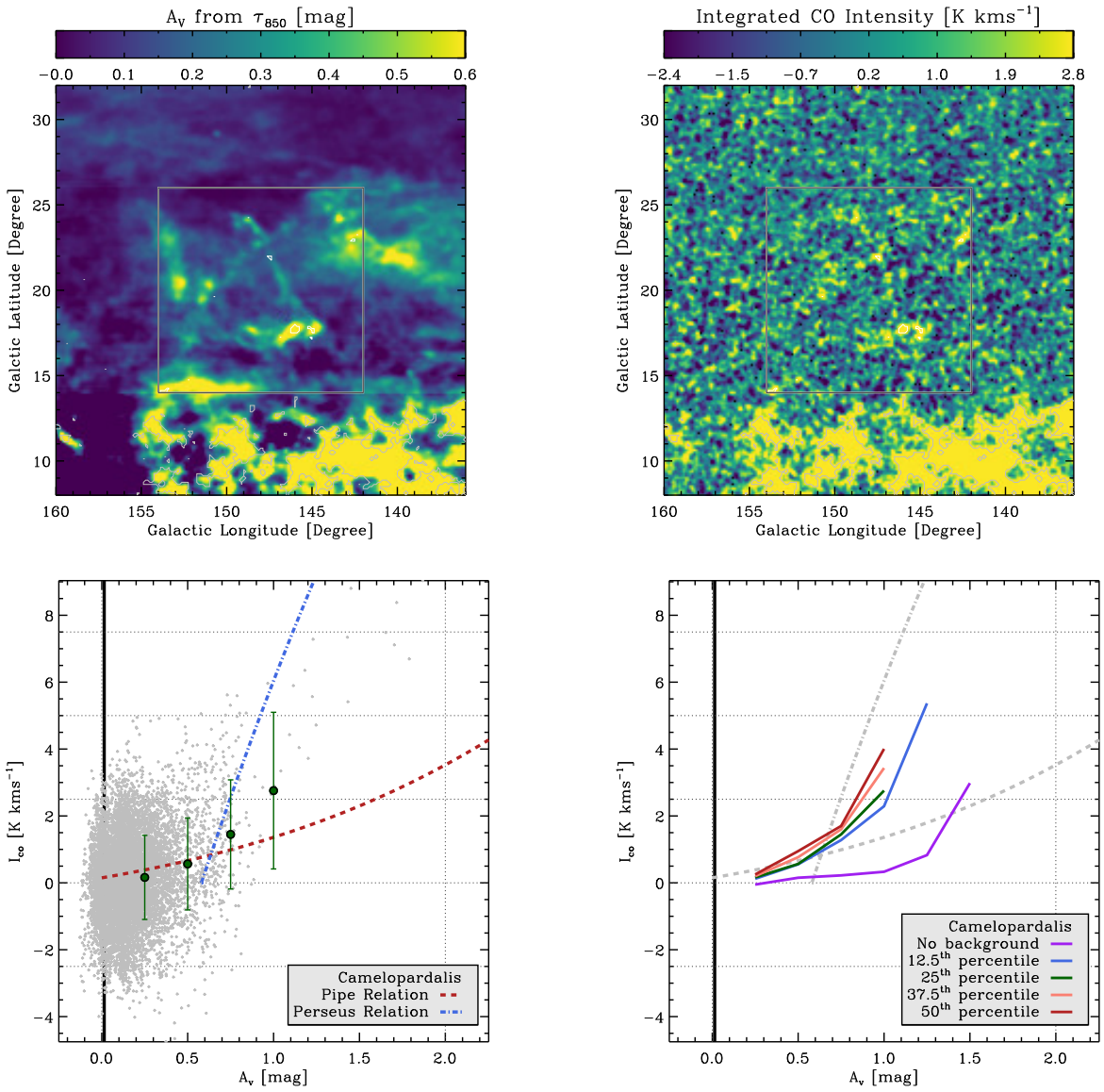

FIG. 12.— Same as Figure 2, for the case of Camelopardalis.

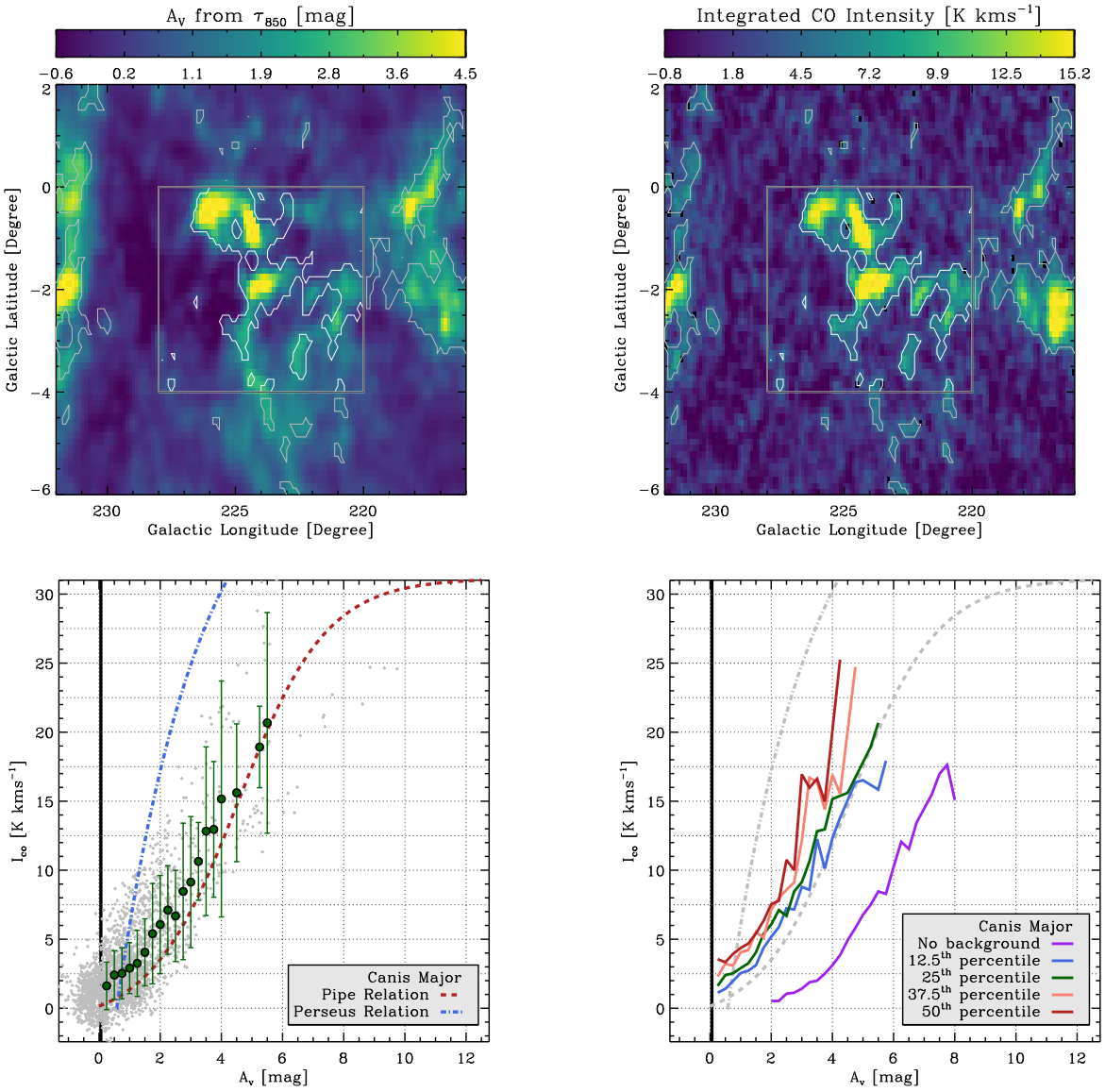

FIG. 13.— Same as Figure 2, for the case of Canis Major.

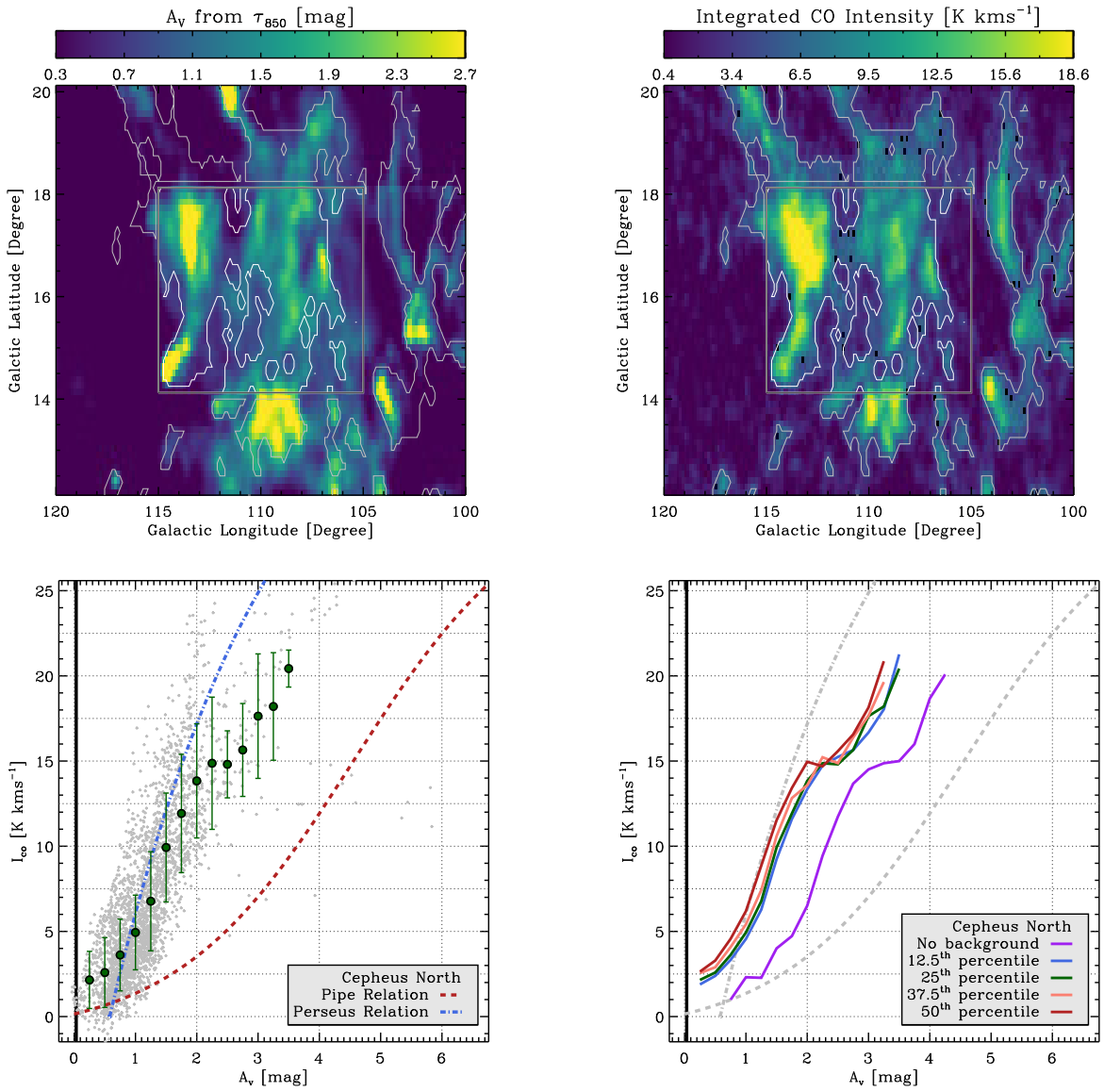

FIG. 14.— Same as Figure 2, for the case of Cepheus North.

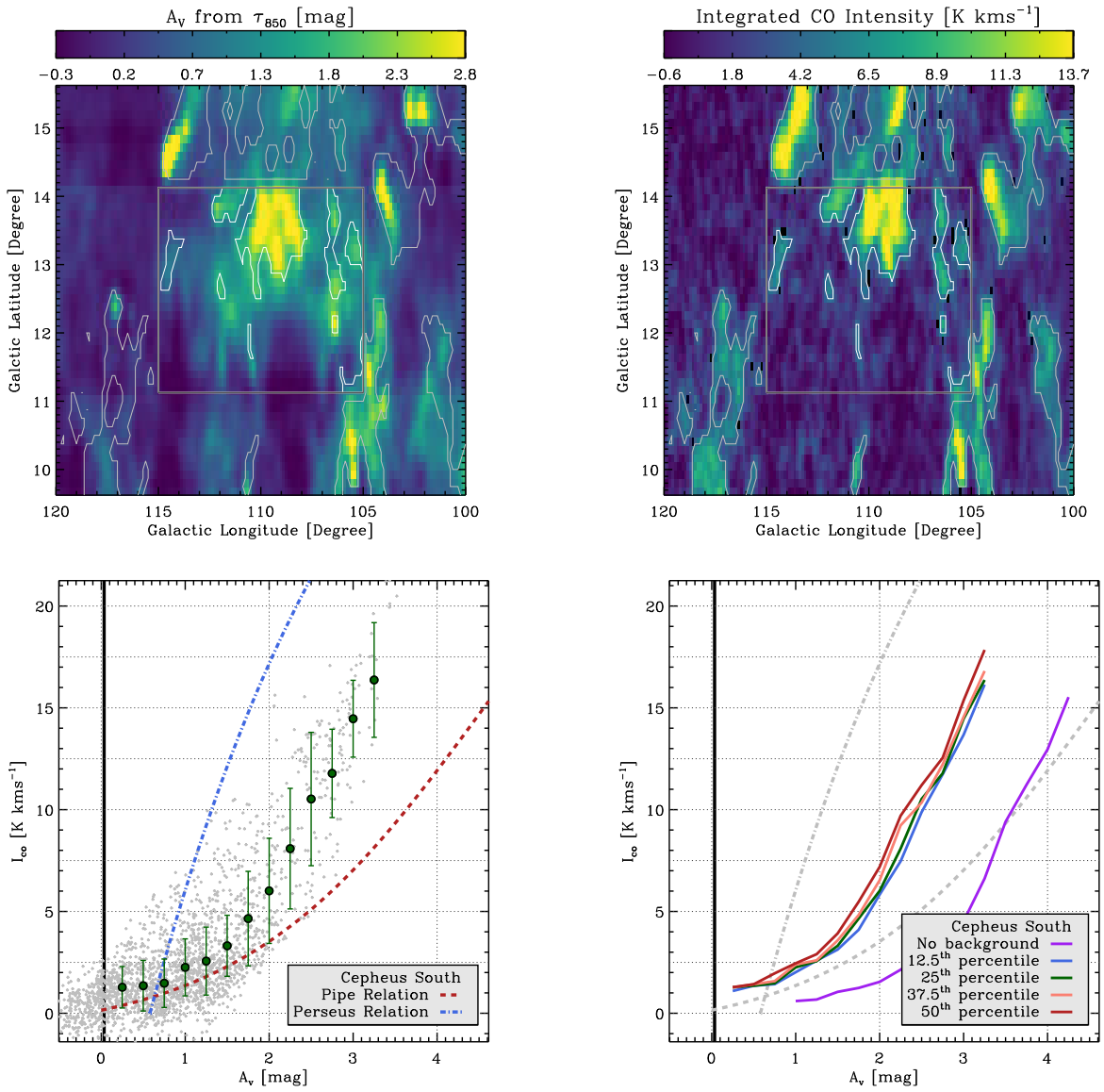

FIG. 15.— Same as Figure 2, for the case of Cepheus South.

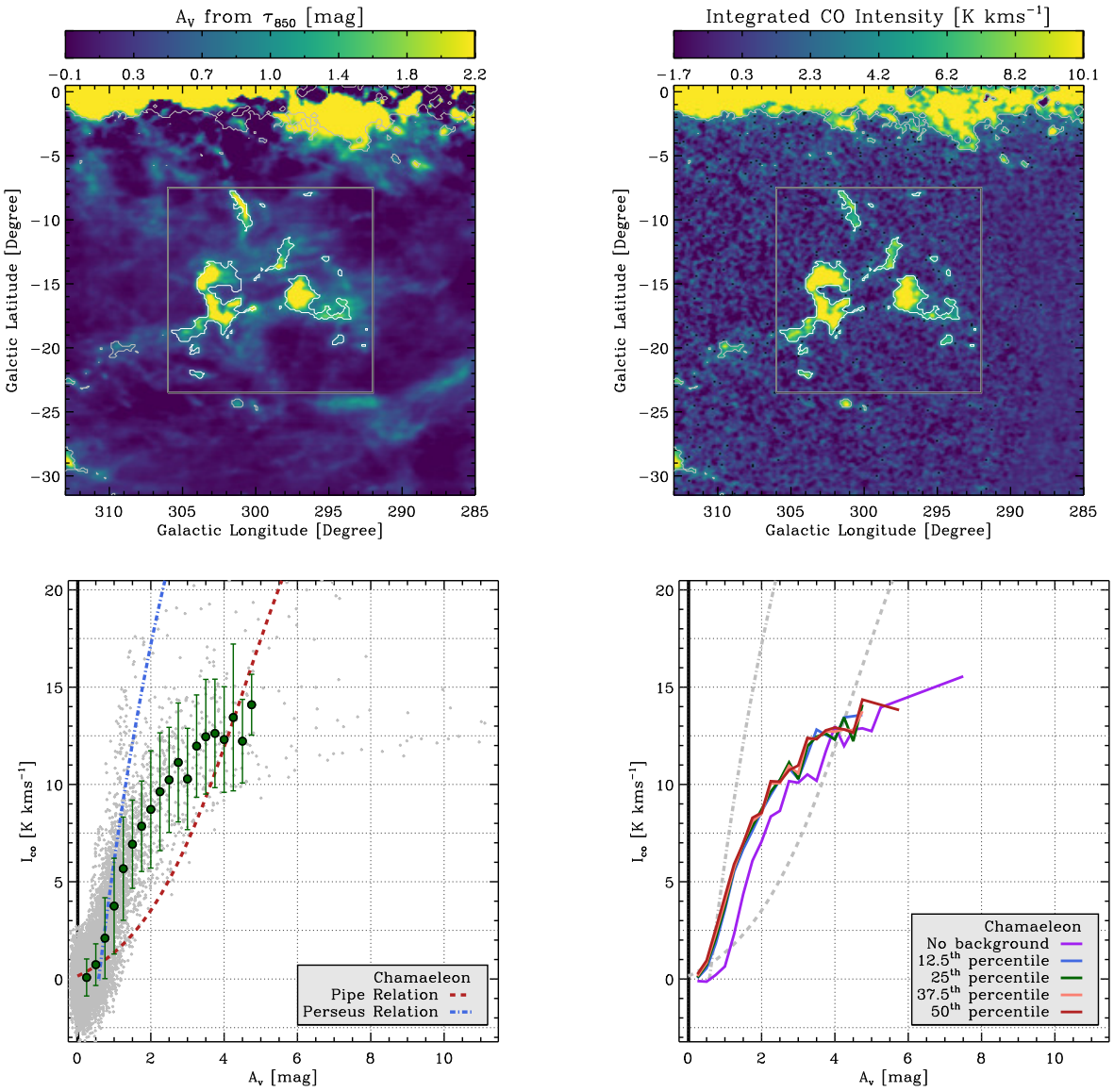

FIG. 16.— Same as Figure 2, for the case of Chamaeleon.

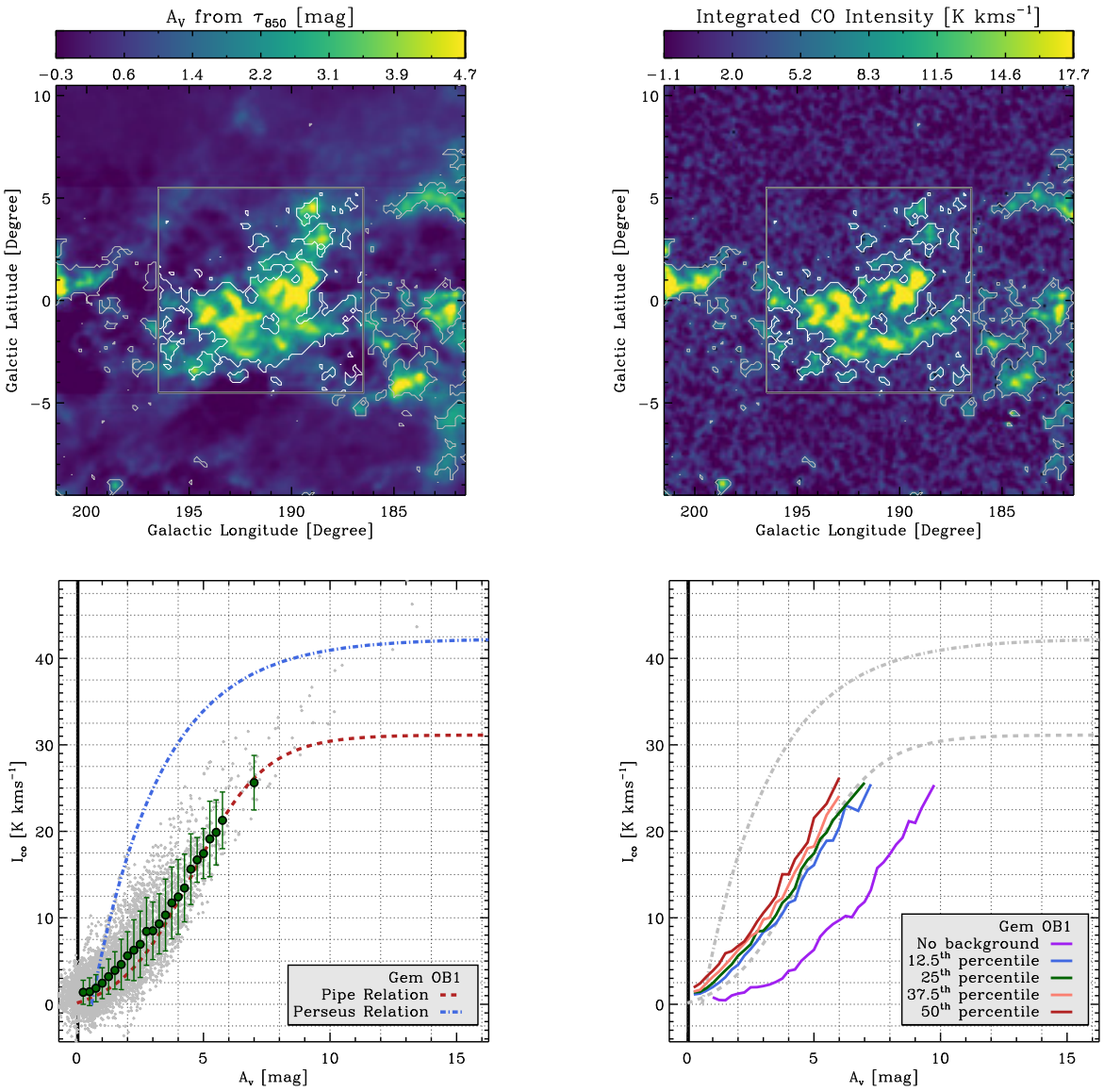

FIG. 17.— Same as Figure 2, for the case of Gem OB1.

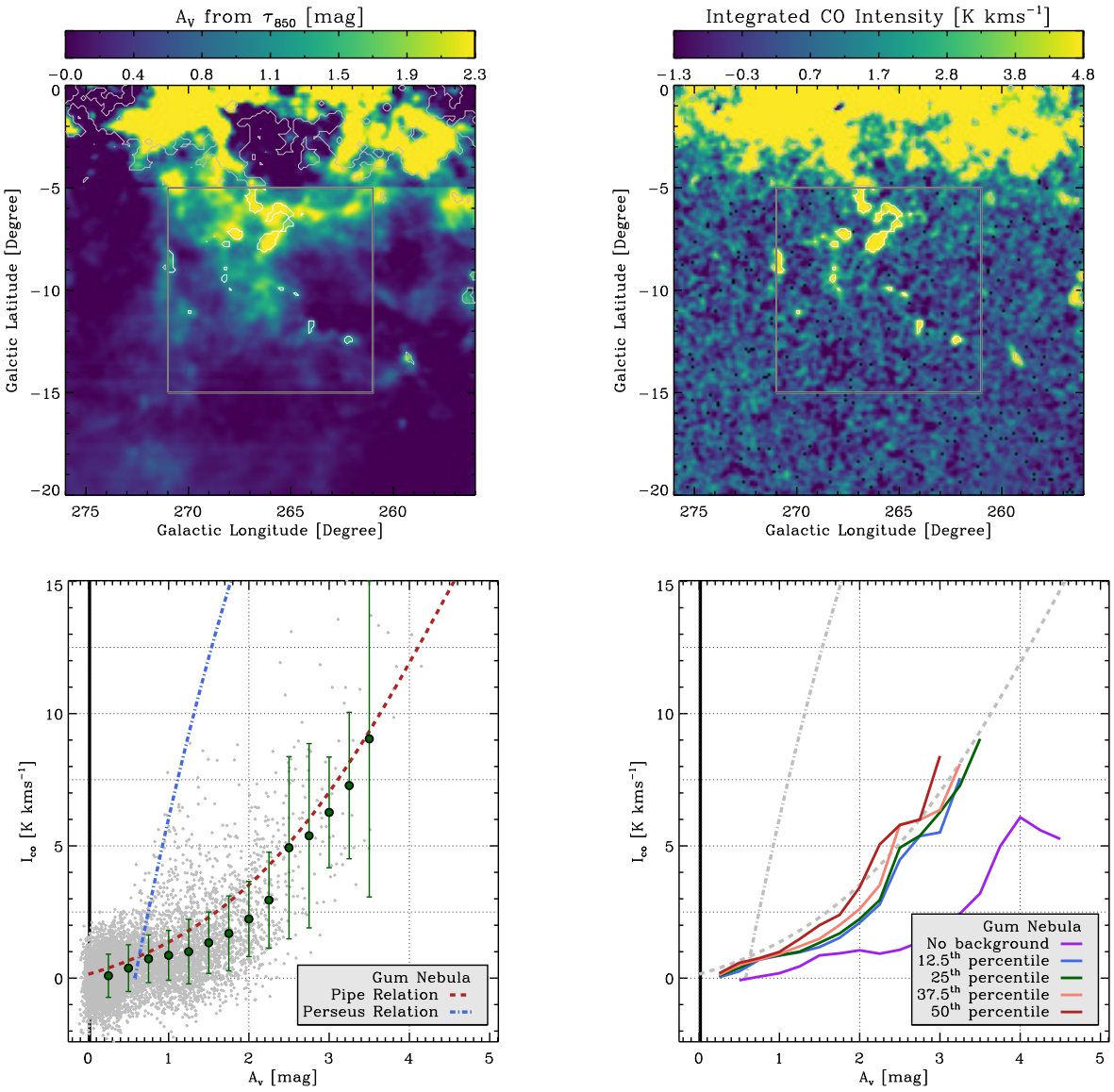

FIG. 18.— Same as Figure 2, for the case of Gum Nebula.

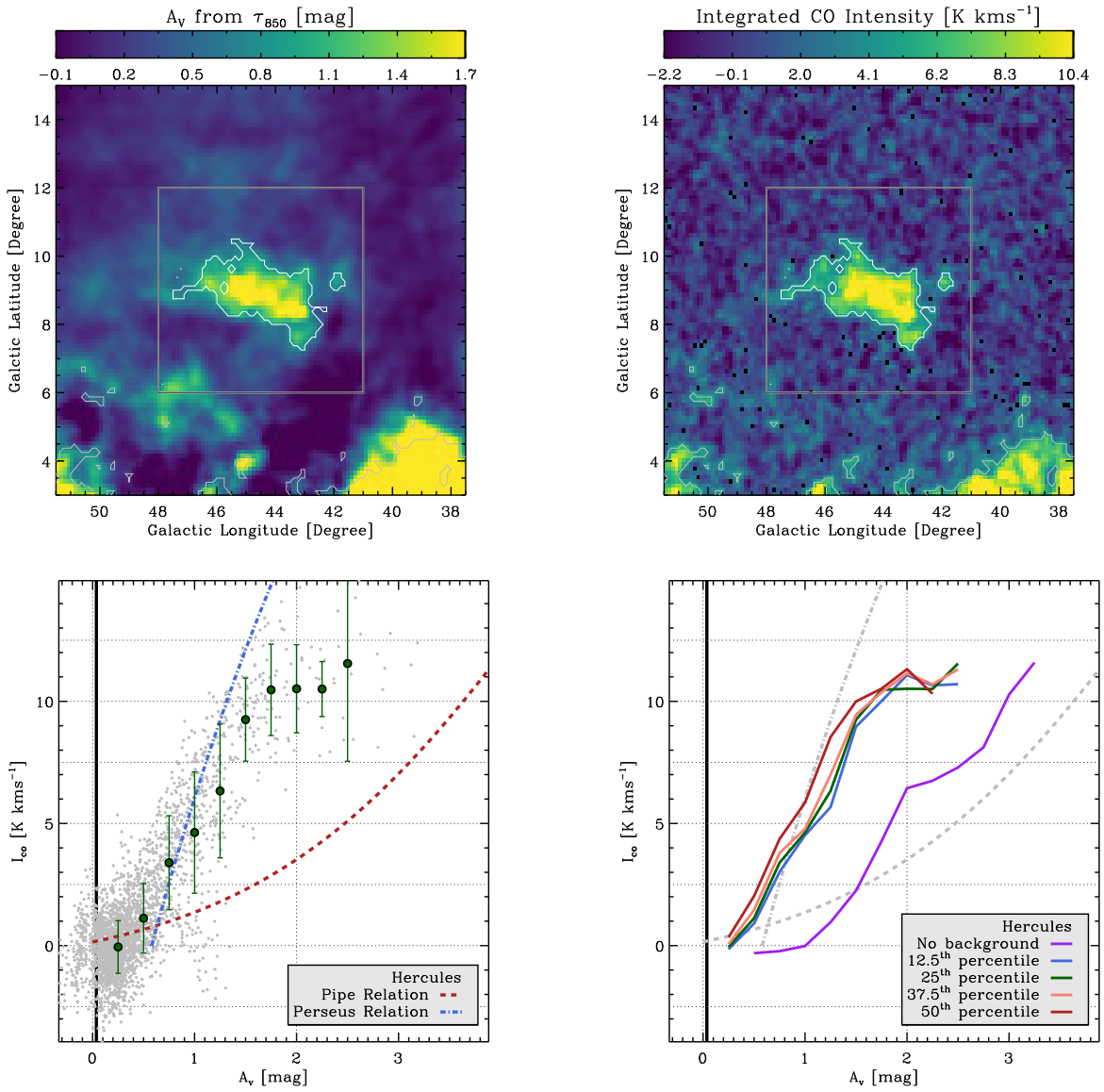

FIG. 19.— Same as Figure 2, for the case of Hercules.

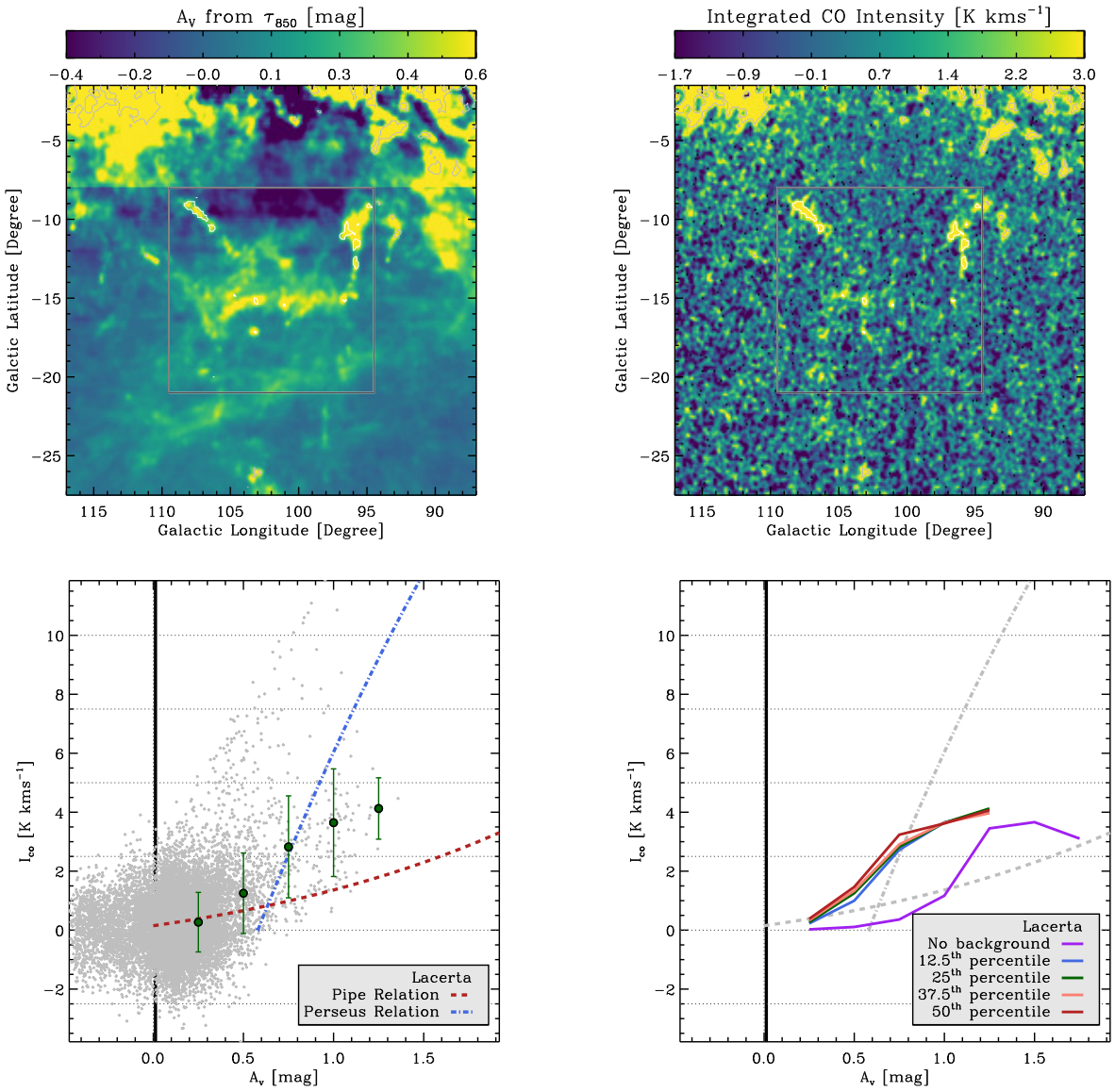

FIG. 20.— Same as Figure 2, for the case of Lacerta.

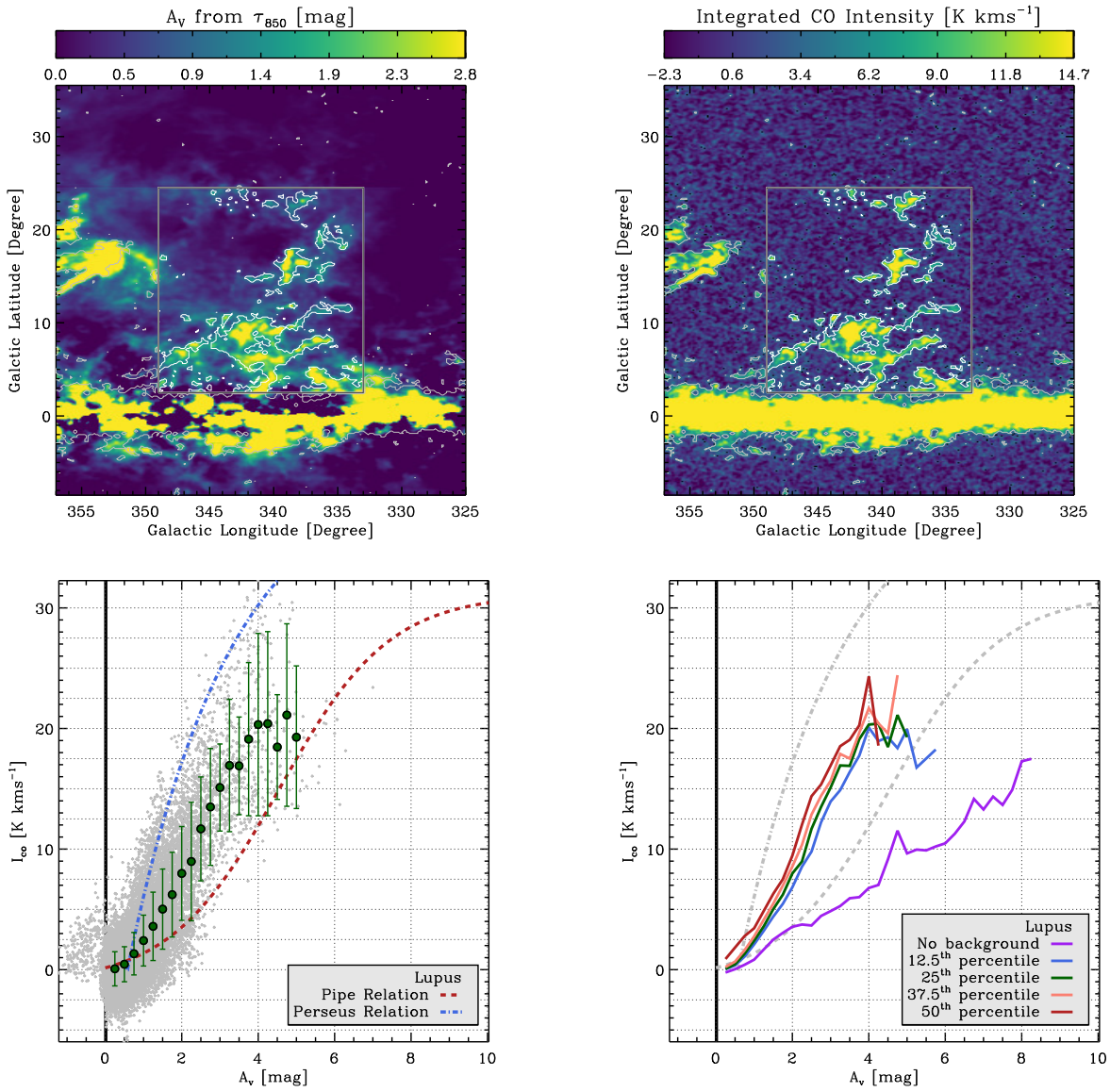

FIG. 21.— Same as Figure 2, for the case of Lupus.

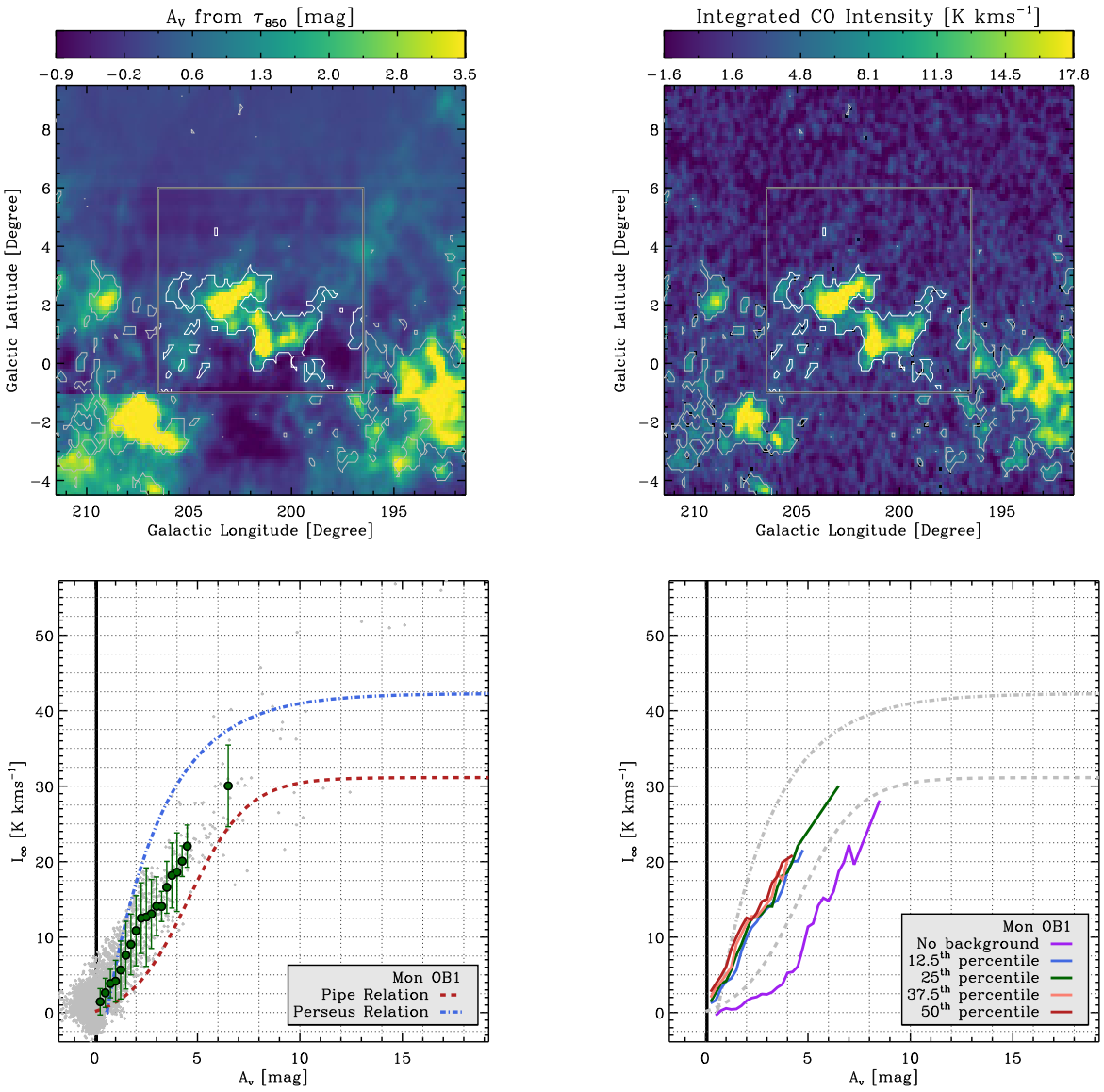

FIG. 22.— Same as Figure 2, for the case of Mon OB1.

REFERENCES

Abreu-Vicente, J., Kainulainen, J., Stutz, A., Henning, T., & Beuther, H. 2015, A&A, 581, A74
Bell, T. A., Roueff, E., Viti, S., & Williams, D. A. 2006, MNRAS, 371, 1865
Bohlin, R. C., Savage, B. D., & Drake, J. F. 1978, ApJ, 224, 132
Bolatto, A. D., Leroy, A. K., Rosolowsky, E., Walter, F., & Blitz, L. 2008, ApJ, 686, 948
Bolatto, A. D., Wolfire, M., & Leroy, A. K. 2013, ARA&A, 51, 207
Boulanger, F., Bronfman, L., Dame, T. M., & Thaddeus, P. 1998, A&A, 332, 273
Carpenter, J. M., Snell, R. L., & Schloerb, F. P. 1995, ApJ, 445, 246
Clark, P. C., & Glover, S. C. O. 2014, MNRAS, 444, 2396
Dame, T. M., Hartmann, D., & Thaddeus, P. 2001, ApJ, 547, 792
Dickman, R. L. 1978, ApJS, 37, 407
Draine, B. T. 1978, ApJS, 36, 595
Glover, S. C. O., & Clark, P. C. 2012a, MNRAS, 421, 116
—. 2012b, MNRAS, 421, 9
—. 2016, MNRAS, 456, 3596
Glover, S. C. O., & Mac Low, M.-M. 2011, MNRAS, 412, 337
Imara, N., & Blitz, L. 2007, ApJ, 662, 969
Israel, F. P. 1997, A&A, 328, 471
Kainulainen, J., Beuther, H., Henning, T., & Plume, R. 2009, A&A, 508, L35
Krumholz, M. R., McKee, C. F., & Tumlinson, J. 2009, ApJ, 693, 216
Lee, C., Leroy, A. K., Schnee, S., et al. 2015, MNRAS, 450, 2708
Lee, M.-Y., Stanimirović, S., Wolfire, M. G., et al. 2014, ApJ, 784, 80
Lee, M.-Y., Stanimirović, S., Douglas, K. A., et al. 2012, ApJ, 748, 75
Lequeux, J., Le Bourlot, J., Pineau des Forets, G., et al. 1994, A&A, 292, 371
Leroy, A. K., Bolatto, A., Bot, C., et al. 2009, ApJ, 702, 352
Leroy, A. K., Bolatto, A., Gordon, K., et al. 2011, ApJ, 737, 12
Liszt, H. S. 1982, ApJ, 262, 198
Liszt, H. S., & Pety, J. 2012, A&A, 541, A58
Lombardi, M., Alves, J., & Lada, C. J. 2006, A&A, 454, 781
—. 2011, A&A, 535, A16
—. 2015, ArXiv e-prints, arXiv:1502.03859
Lombardi, M., Lada, C. J., & Alves, J. 2008, A&A, 489, 143
—. 2010, A&A, 512, A67
Maloney, P., & Black, J. H. 1988, ApJ, 325, 389
Pineda, J. E., Caselli, P., & Goodman, A. A. 2008, ApJ, 679, 481
Pineda, J. L., Goldsmith, P. F., Chapman, N., et al. 2010, ApJ, 721, 686
Planck Collaboration, Ade, P. A. R., Aghanim, N., et al. 2013a, ArXiv e-prints, arXiv:1303.5073

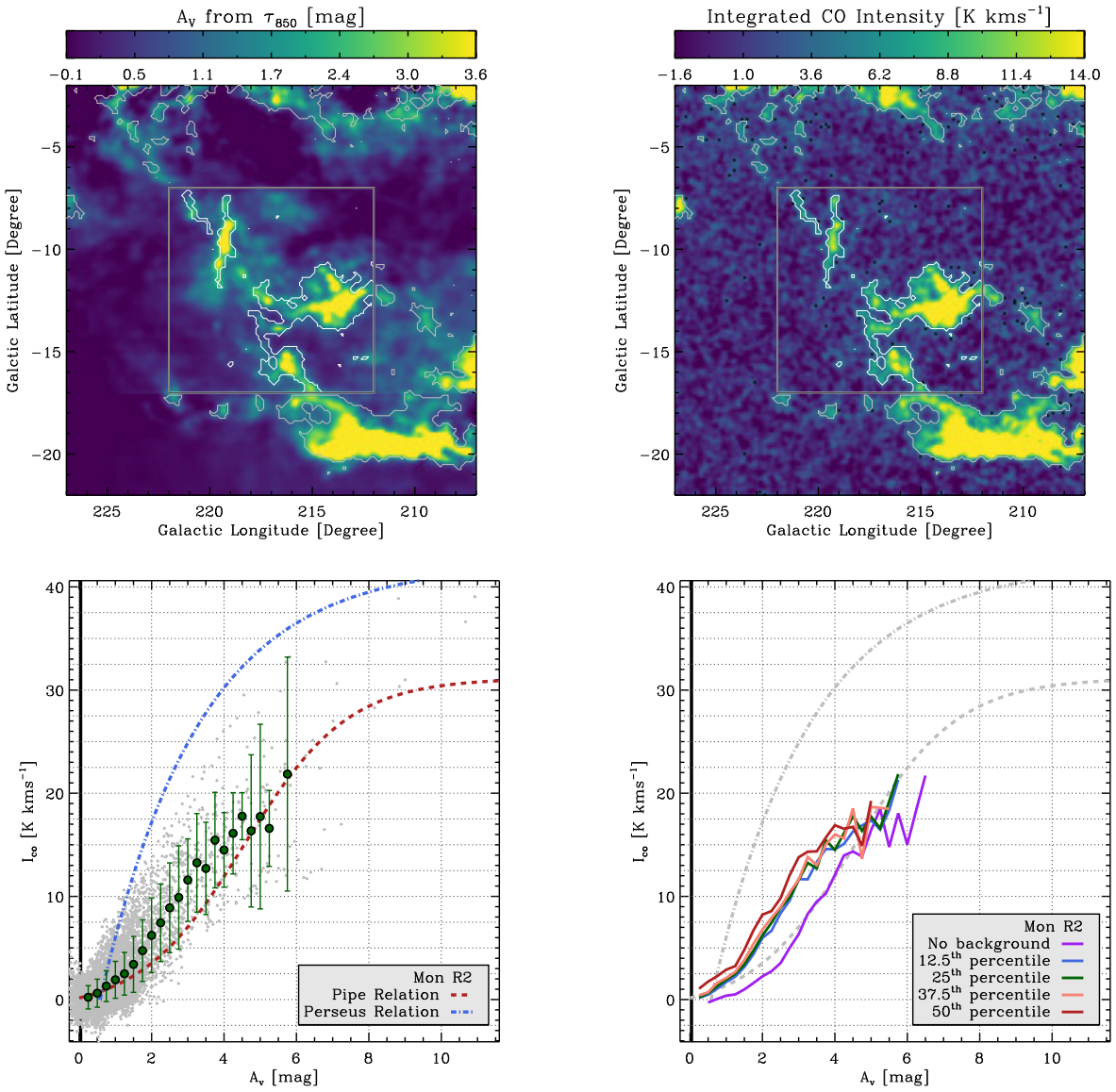

FIG. 23.— Same as Figure 2, for the case of Mon R2.

Planck Collaboration, Abergel, A., Ade, P. A. R., et al. 2013b, ArXiv e-prints, arXiv:1312.1300

Reipurth, B. 2008, Handbook of Star Forming Regions, Volume I: The Northern Sky

Rémy-Ruyer, A., Madden, S. C., Galliano, F., et al. 2014, A&A, 563, A31

Rosolowsky, E., Engargiola, G., Plambeck, R., & Blitz, L. 2003, ApJ, 599, 258

Sandstrom, K. M., Leroy, A. K., Walter, F., et al. 2013, ApJ, 777, 5

Schlafly, E. F., Green, G., Finkbeiner, D. P., et al. 2014, ApJ, 786, 29

Schneider, N., Ossenkopf, V., Csengeri, T., et al. 2015, A&A, 575, A79

Schruba, A., Leroy, A. K., Walter, F., et al. 2012, AJ, 143, 138

Schruba, A., Leroy, A. K., Kruijssen, J. M. D., et al. 2017, ApJ, 835, 278

Sheffer, Y., Rogers, M., Federman, S. R., et al. 2008, ApJ, 687, 1075

Shetty, R., Glover, S. C., Dullemond, C. P., & Klessen, R. S. 2011, MNRAS, 412, 1686

Springel, V. 2005, MNRAS, 364, 1105

Sternberg, A., Le Petit, F., Roueff, E., & Le Bourlot, J. 2014, ApJ, 790, 10

Tielens, A. G. G. M., & Hollenbach, D. 1985, ApJ, 291, 722

van Dishoeck, E. F., & Black, J. H. 1988, ApJ, 334, 771

Visser, R., van Dishoeck, E. F., & Black, J. H. 2009, A&A, 503, 323

Wilson, C. D. 1995, ApJ, 448, L97

Wolfire, M. G., Hollenbach, D., & McKee, C. F. 2010, ApJ, 716, 1191

Young, J. S., & Scoville, N. 1982, ApJ, 258, 467

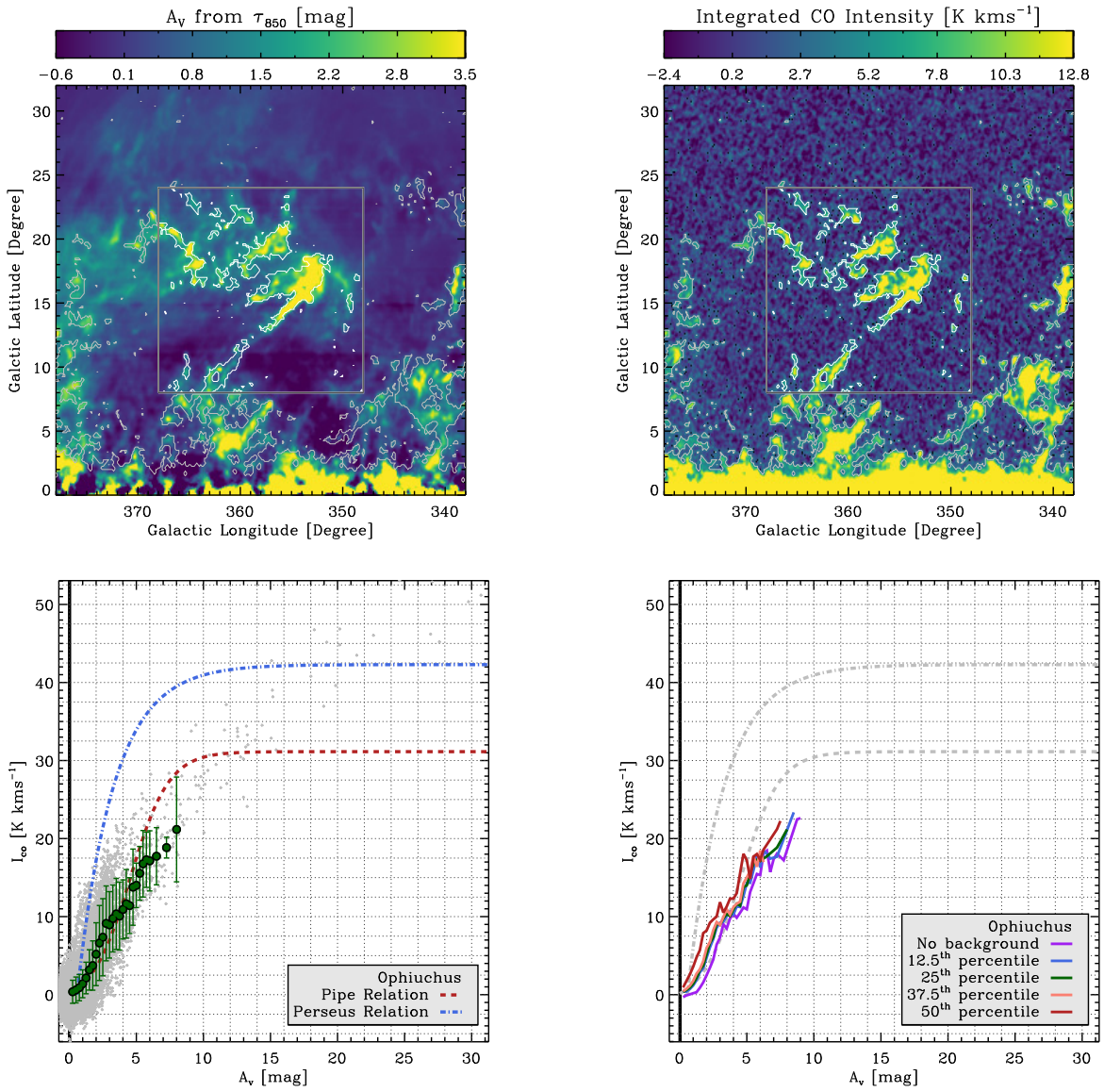

FIG. 24.— Same as Figure 2, for the case of Ophiuchus.

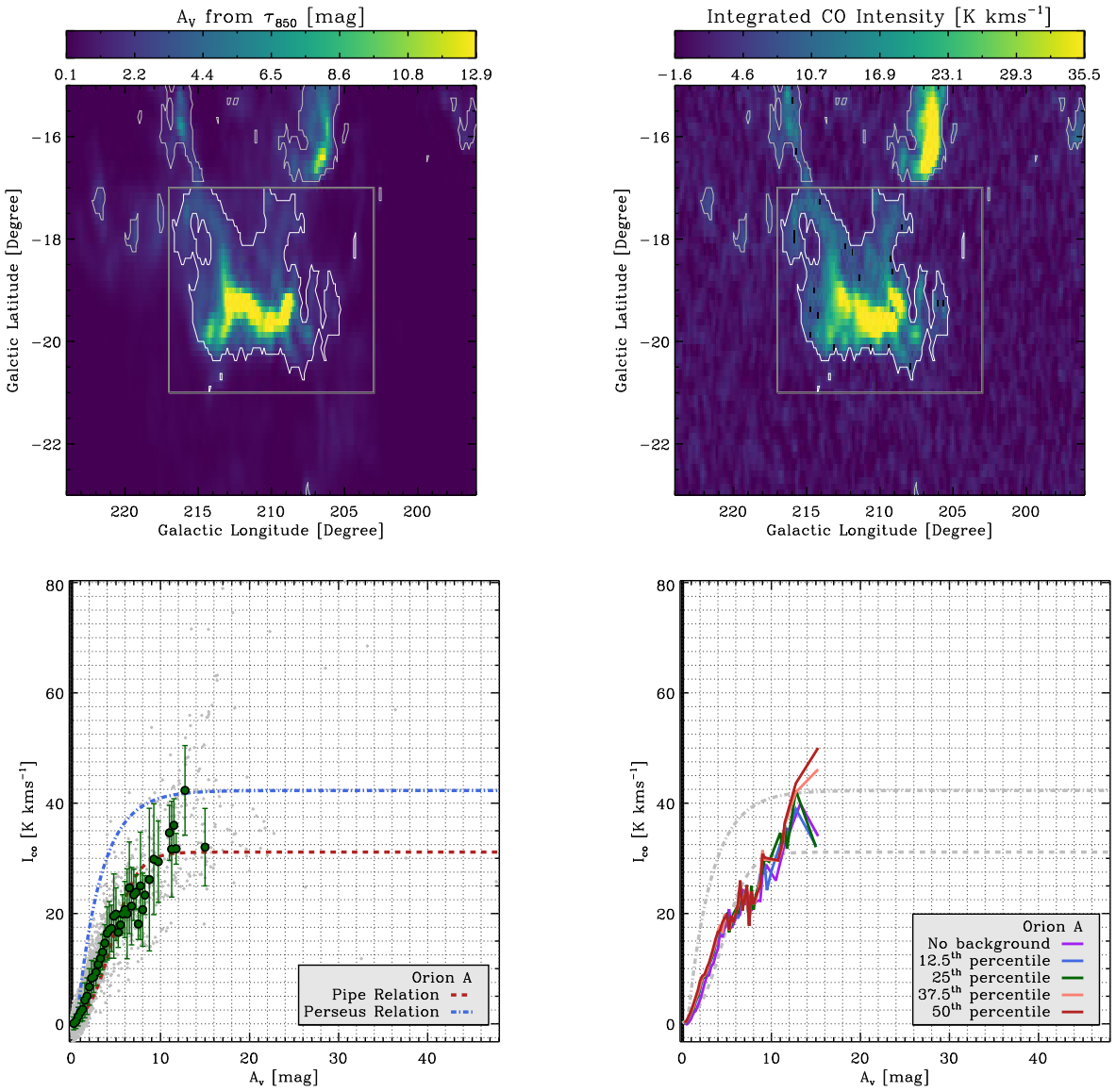

FIG. 25.— Same as Figure 2, for the case of Orion A.

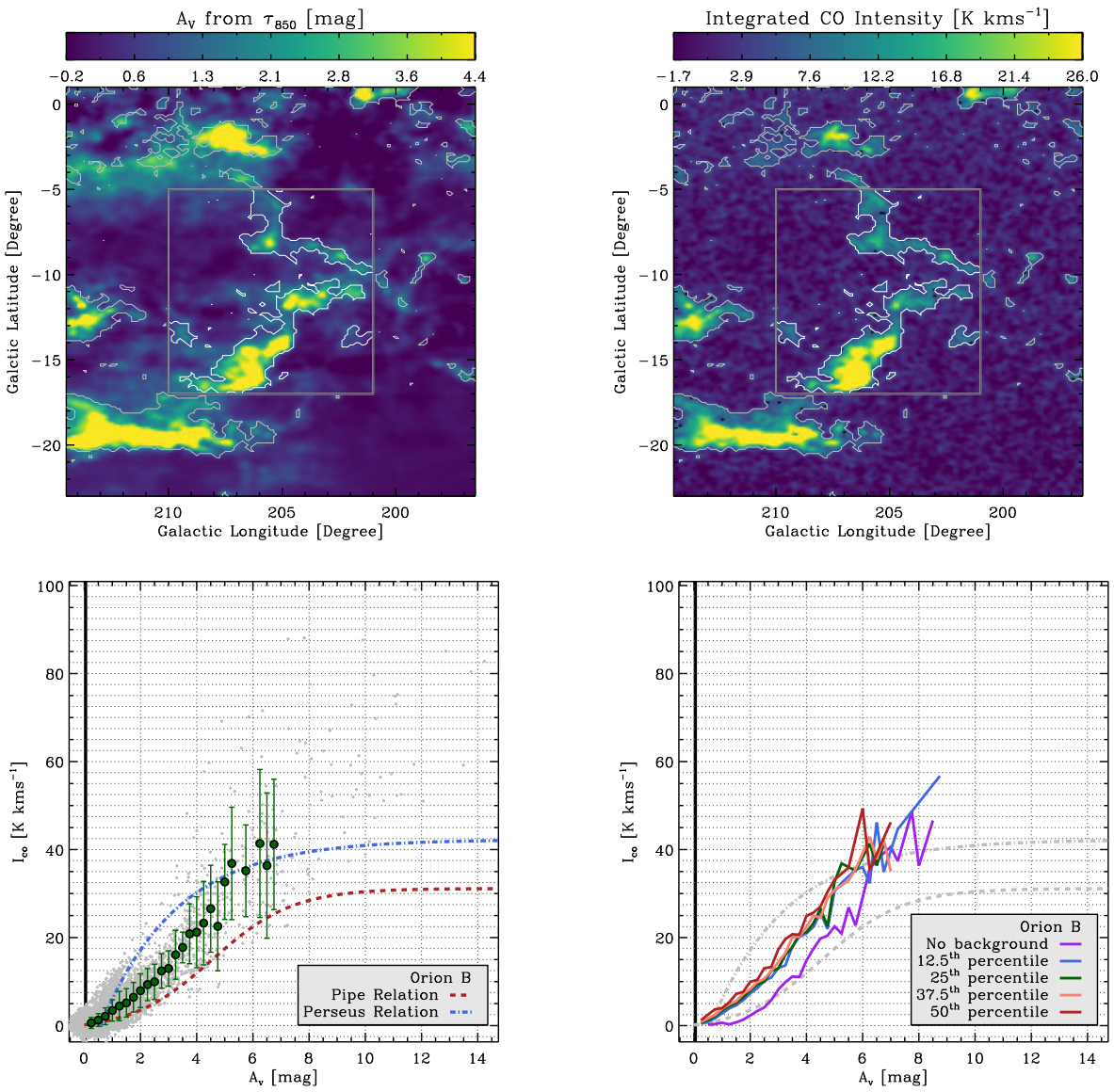

FIG. 26.— Same as Figure 2, for the case of Orion B.

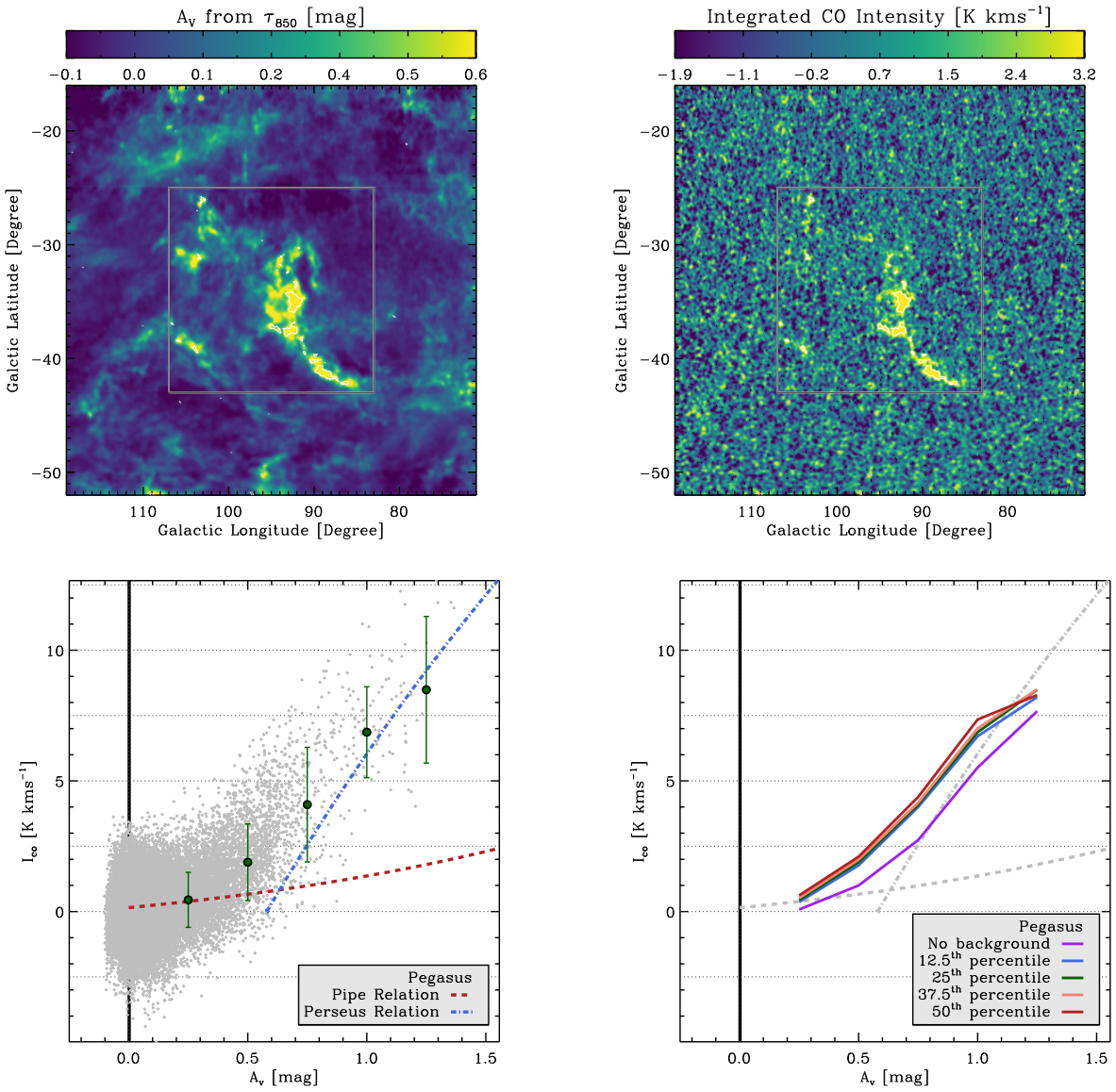

FIG. 27.— Same as Figure 2, for the case of Pegasus.

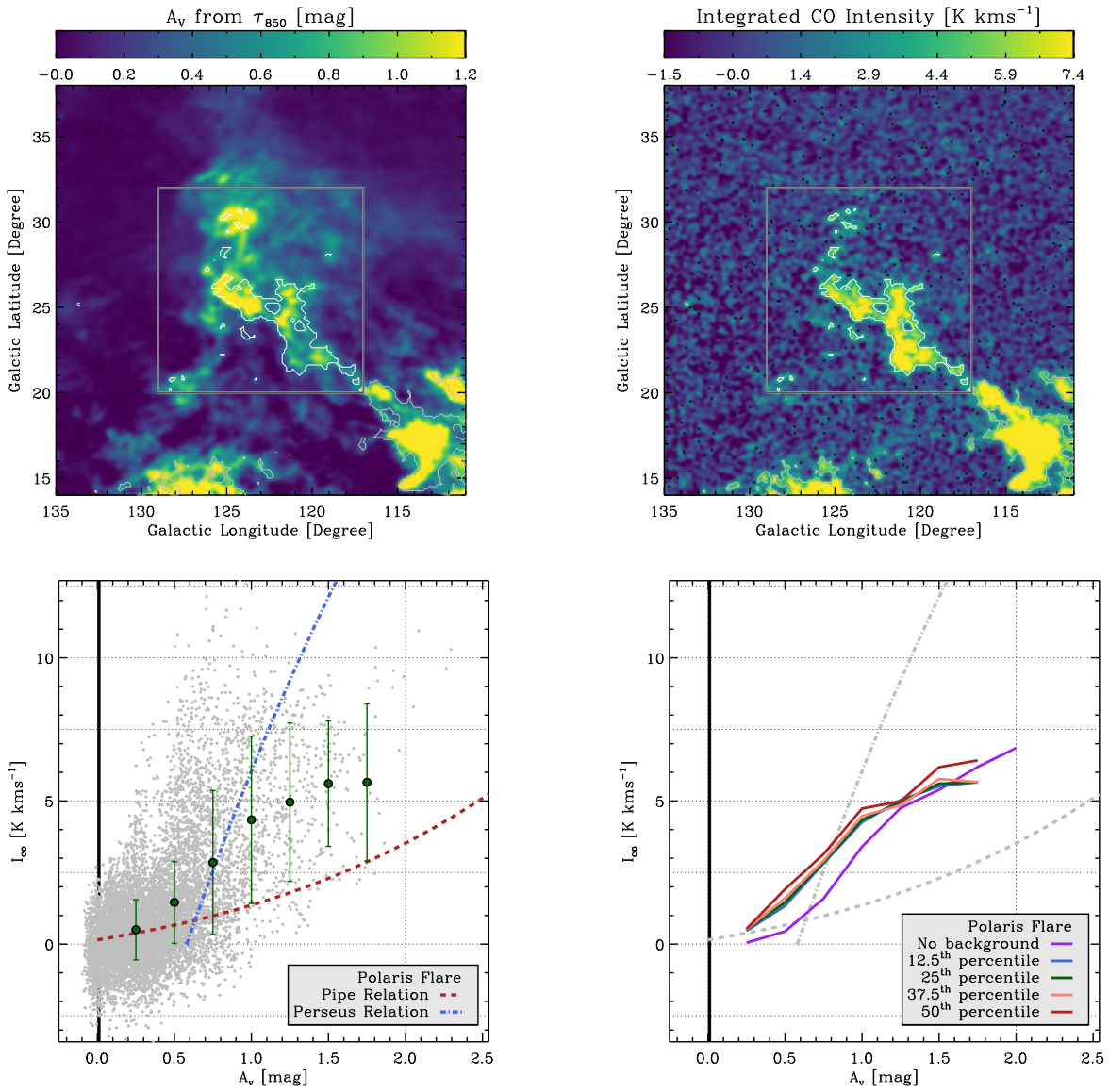

FIG. 28.— Same as Figure 2, for the case of Polaris Flare.

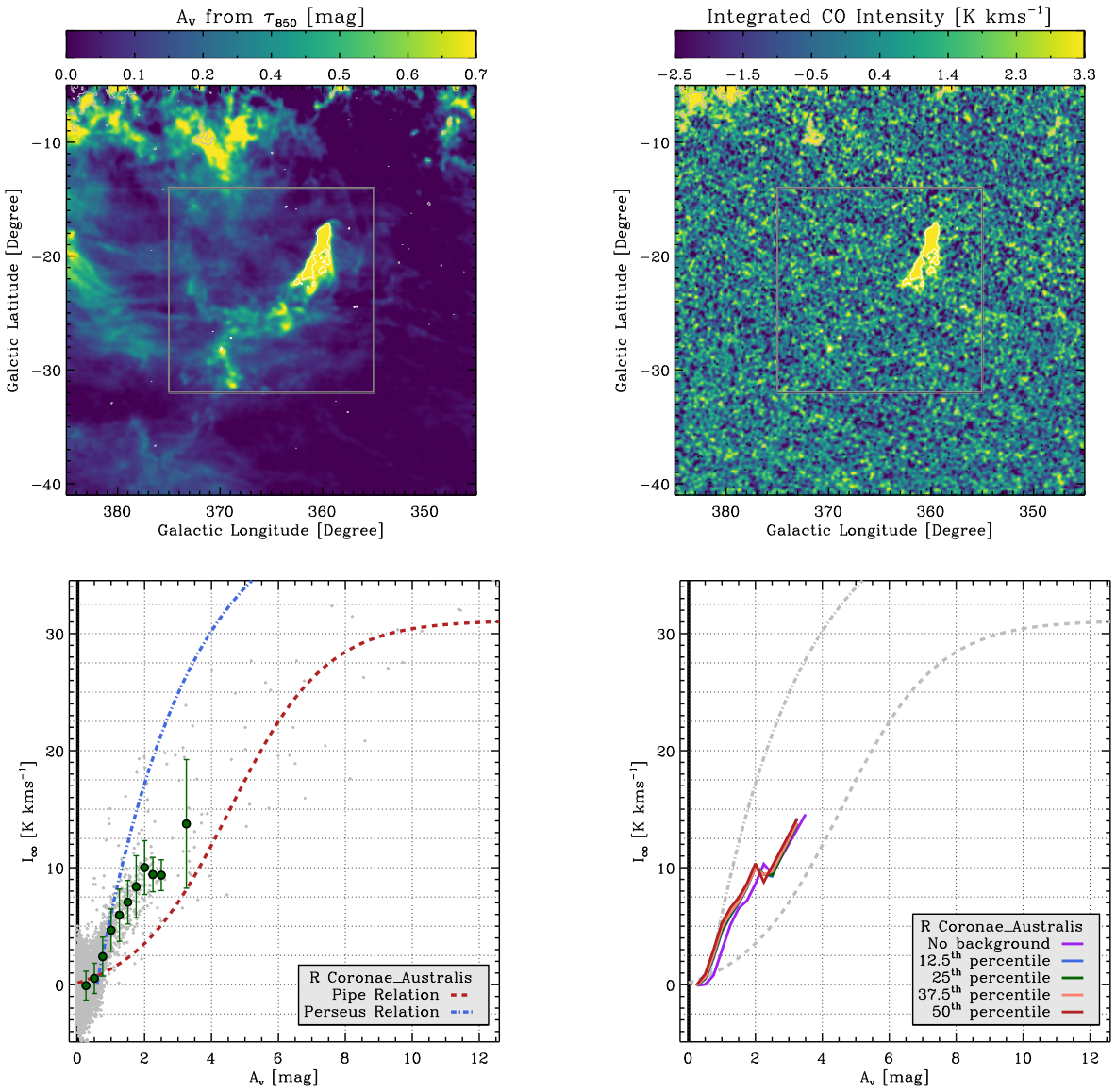

FIG. 29.— Same as Figure 2, for the case of R Coronae Australis.

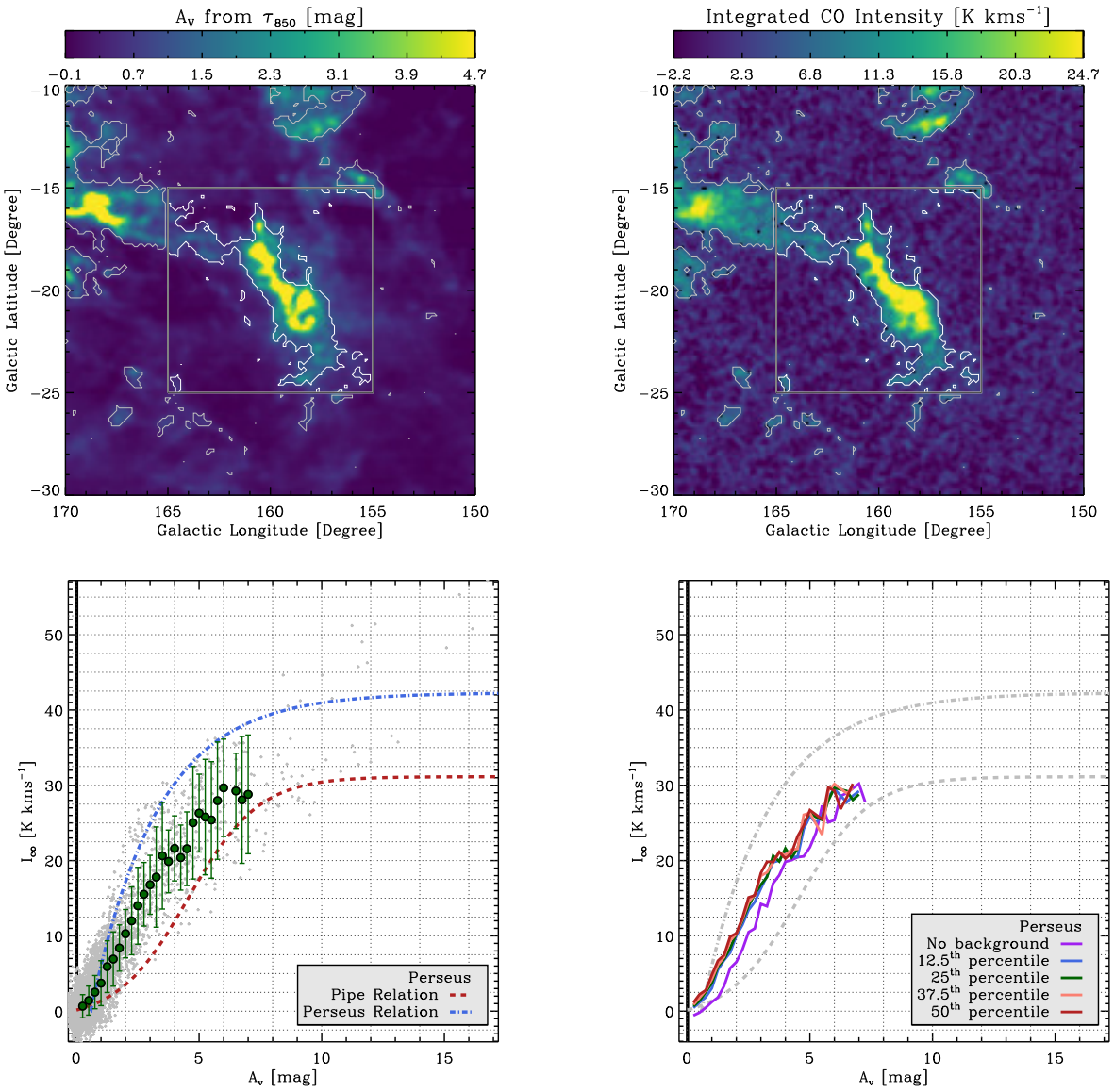

FIG. 30.— Same as Figure 2, for the case of Perseus.

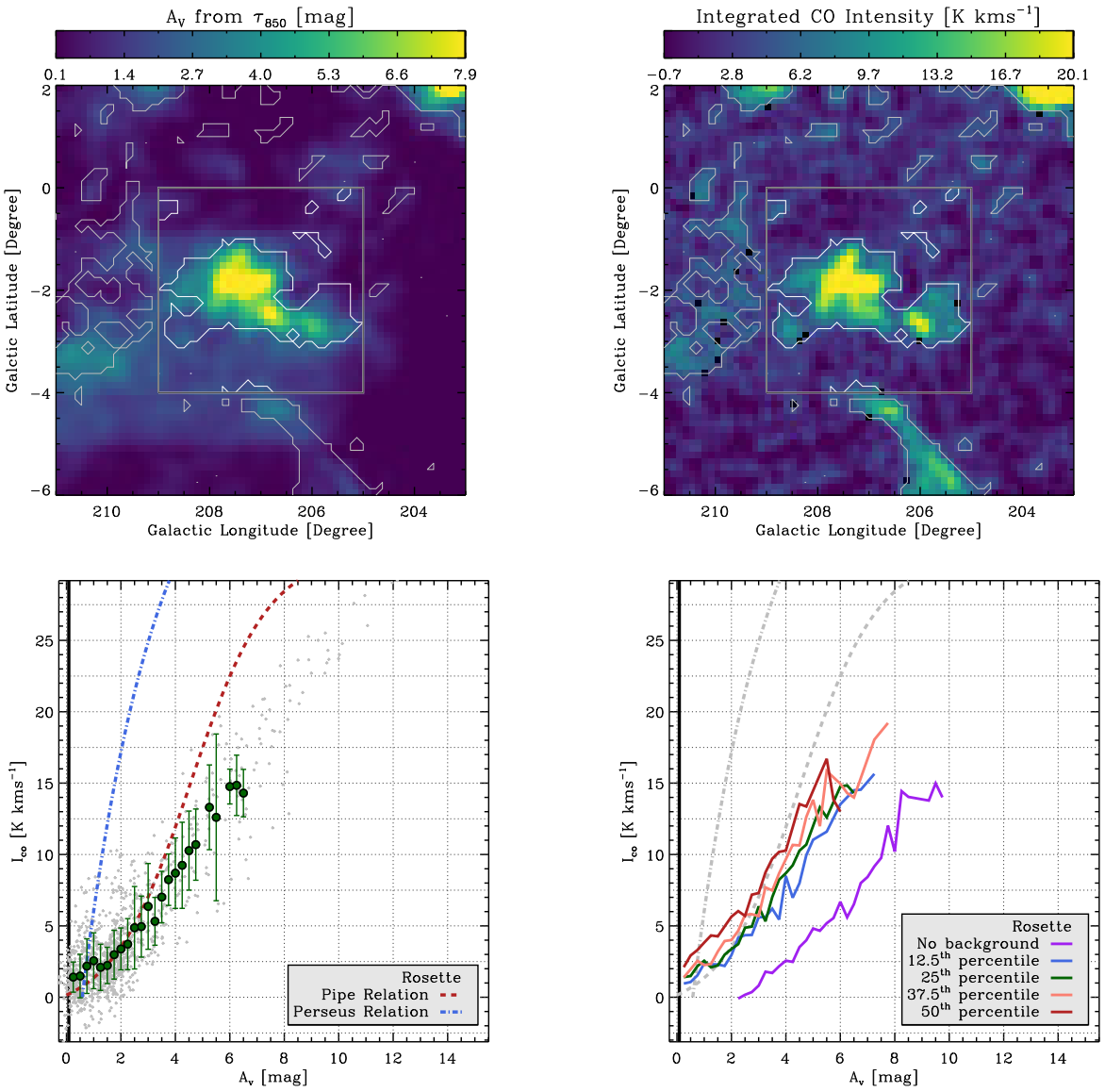

FIG. 31.— Same as Figure 2, for the case of Rosette.